

# Hydrothermal fluid signatures of the Yulong porphyry Cu-Mo deposit: Clues from the composition and U-Pb dating of W-bearing rutile

QI CHEN<sup>1</sup>, CHANGMING WANG<sup>1,\*</sup>, LEON BAGAS<sup>1,2</sup>, BIN DU<sup>1,3</sup>, KANGXING SHI<sup>1</sup>, AND JIAXUAN ZHU<sup>1</sup>

<sup>1</sup>State Key Laboratory of Geological Processes and Mineral Resources, China University of Geosciences (Beijing), Beijing 100083, China

<sup>2</sup>Xi'an Center of Mineral Resources Survey, China Geological Survey, Xi'an 710054, China

<sup>3</sup>China Non-ferrous Metals Resource Geological Survey, Beijing 100012, China

## ABSTRACT

Hydrothermal rutile (TiO<sub>2</sub>) is a widely distributed accessory mineral in hydrothermal veins or alteration assemblages of porphyry deposits and provides important information for further understanding hydrothermal fluid signatures. This study determines the geochemical composition and U-Pb dates of hydrothermal rutile from the Yulong porphyry Cu-Mo deposit in east Tibet, China. Three types of TiO<sub>2</sub> polymorphs have been identified based on their Raman spectroscopic, textural, and chemical characteristics. (1) Brookite and anatase pseudomorphs after titanite in a fine-grained matrix, indicating low-temperature hydrothermal fluids destabilizing primary Ti-bearing minerals during argillic alteration (type-I). (2) Elongated and prismatic rutile present in hydrothermal veins or in clusters in accompanying alteration envelope characterized by weak zoning (type-II). And (3) rutile intergrown with sulfides in hydrothermal veins, characterized by well-developed patchy and sector zoning (type-III). In contrast to the type-I and type-II TiO<sub>2</sub> polymorphs, tungsten is enriched in backscattered bright patches and sector zones in type-III rutile, which is due to the substitution of W<sup>6+</sup> in the Ti<sup>4+</sup> octahedral site. The mechanism of the enrichment of tungsten is effectively driven by the halogen-rich (F, Cl) aqueous fluids during hydrothermal mineralization. In situ U-Pb dating of the type-III rutile yields a lower intercept age of 41.8 ± 1.2 Ma, which brackets the timing of the Cu-Mo mineralization. The relationship between rutile textures and composition indicates that W-bearing rutile can serve as a recorder of hydrothermal processes in porphyry Cu deposits.

**Keywords:** W-bearing rutile, hydrothermal fluid signatures, U-Pb geochronology, EMPA, mineral chemistry, porphyry Cu-Mo deposits

## INTRODUCTION

Rutile is a widely distributed accessory mineral, found in metamorphic, sedimentary, and igneous rocks (Zack et al. 2004; Meinhold 2010; Zack and Kooijman 2017; Pe-Piper et al. 2019) and formed in many magmatic-hydrothermal ore deposits, such as porphyry deposits (Scott 2005; Rabbia et al. 2009; Schirra and Laurent 2021; Wang et al. 2021). Previous studies have confirmed that rutile can form as a replacement product of Ti-bearing oxides and silicates (such as ilmenite, titanite, or biotite), and contains variable concentrations of Fe, V, high field strength elements (HFSE), transition, and base metallic elements (Luvizotto and Zack 2009; Meinhold 2010; Plavsa et al. 2018; Agangi et al. 2019). The variable concentrations of trace elements are closely connected to the composition of the primary minerals, type and composition of magmatic and metamorphic fluids (Cl- or F-rich), pressure and temperature conditions, and oxygen fugacity ( $f_{O_2}$ ) (Zack et al. 2002, 2004; Plavsa et al. 2018; Majzlan et al. 2021). Therefore, rutile enriched in V, W, Mo, Sn, and Sb can be used as a geochemical fingerprint of a hydrothermal fluid associated with mineralization (cf. Czamanske et al. 1981; Clark and Williams-Jones 2004; Scott 2005; Scott et al. 2011; Agangi et al. 2019).

Studies of rutile associated with porphyry Cu deposits have already been attempted using: (1) the trace element signature of the rutile as an indicator of mineralization (Rabbia et al. 2009; Schirra and Laurent 2021), and (2) direct U-Pb dating of rutile associated with sulfides to constrain the timing of the hydrothermal mineralization events (Schirra and Laurent 2021). Studies of variations in, and incorporation mechanism of, these pathfinder elements in rutile in porphyry deposits are still very limited. For example, individual rutile commonly contains well-developed patchy and sector zonation reflecting the distributions of various elements (e.g., W, Fe; Mercer and Reed 2013). Nonetheless, the modification of these elements driven by hydrothermal fluids is poorly understood. Published studies have reported that hydrothermal rutile containing up to 3 wt% tungsten content in porphyry deposits closely coexists with sulfides, such as the Butte deposit in the U.S.A. (Mercer and Reed 2013). However, there is still a lack of understanding of the genesis of W-bearing rutile in hydrothermal veins, including its distribution, substitution mechanism and source of W. Answers to the above-mentioned problems are potentially helpful in understanding the critical contributions of hydrothermal fluids to mineralization in porphyry deposits, and defining vectors to undiscovered systems.

The world-class Yulong Cu-Mo porphyry deposit (Fig. 1) is hosted by an extensional (post-collisional) strike-slip fault

\* E-mail: wangcm@cugb.edu.cn

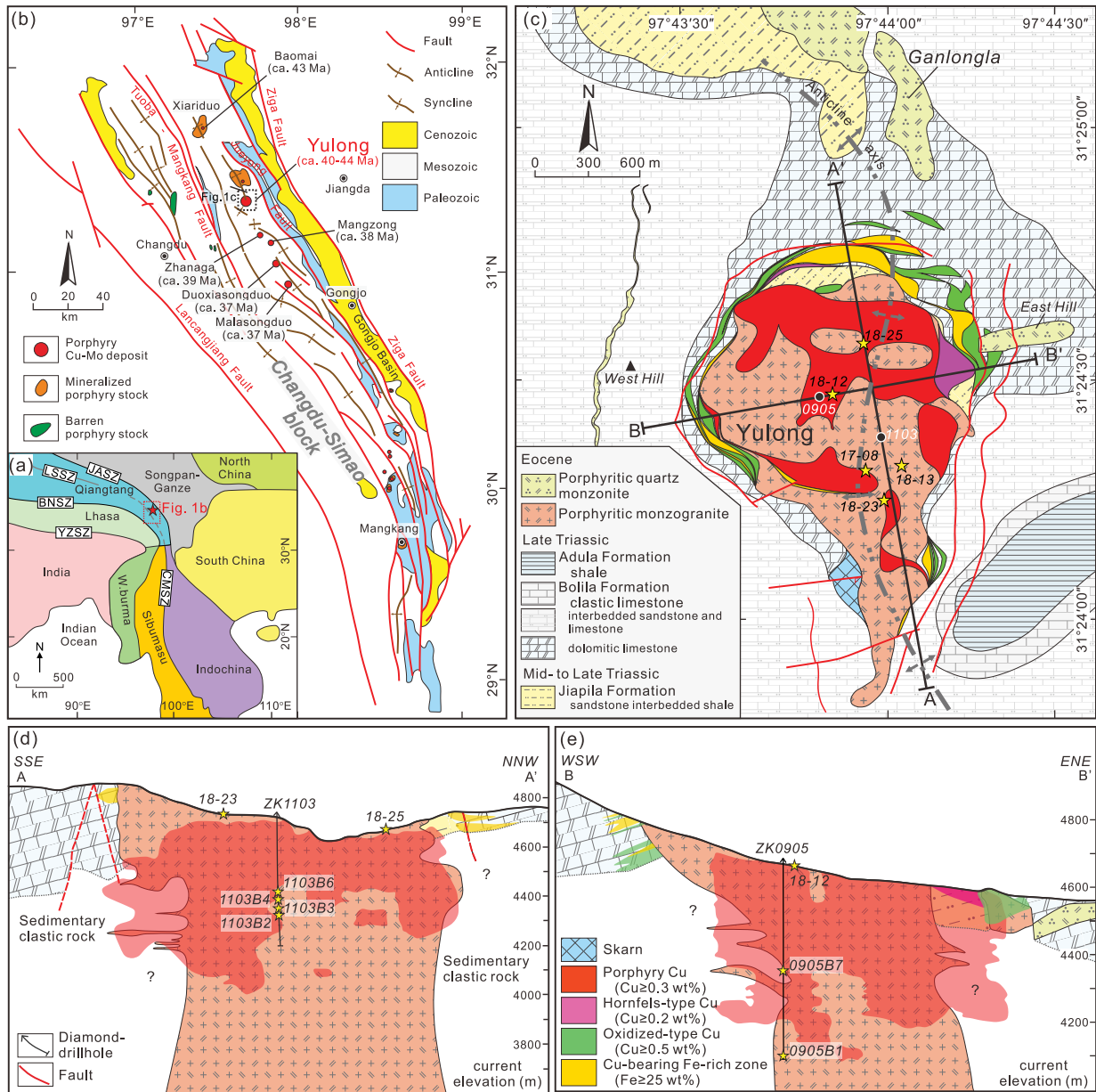


**FIGURE 1.** (a) Simplified tectonic framework of the Sanjiang Orogen and its adjacent areas (modified after Wang et al. 2014); (b) simplified geological map of the Eocene Yulong porphyry Cu belt (modified after Hou et al. 2003); (c) geological map of the Yulong deposit (modified after Chang et al. 2018); and (d–e) distribution and zonation of mineralization based on the logging of drill core along the two cross sections. The figure shows the SSE-NNW oriented cross section A-A' parallel to the long axis and the WSW-ENE oriented cross section B-B' perpendicular to the long axis of the Yulong porphyry (modified after Chang et al. 2017). The pentagrams show the locations of samples analyzed in this study. Abbreviations: JASZ = Jinshajiang-Ailaoshan Suture Zone; LSSZ = Longmu Co-Shuanghu Suture Zone; CMSZ = Changning-Menglian Suture Zone; BNSZ = Bangonghu-Nujiang Suture Zone; YZSZ = Yarlung Zangbo Suture Zone. (Color online.)

zone in eastern Tibet, and has been the focus of extensive studies and exploration in recent years (Tang and Luo 1995; Hou et al. 2003, 2006; Li et al. 2012; Chang et al. 2017, 2018; Huang et al. 2019). Various minerals existing in porphyries, hydrothermal veins or alteration halos have been used to constrain the magmatic and hydrothermal processes operating during the genesis of the deposit (Huang et al. 2019). These include: (1) the accurately

determined age and duration of molybdenite crystallization in the deposit (Chang et al. 2017); (2) the evolution of the mineralizing magmatic-hydrothermal fluids and metal precipitation based on the study of fluid inclusions in quartz (Sun et al. 2021); and (3) constraints on the timescales of individual magmatic phases and fluid pulses using Ti diffusion in quartz (Chen et al. 2021). Although rutile is abundant in altered porphyries and hydrothermal veins

that are closely related to mineralization, its origins, mineralogical characteristics, and the nature of mineralization processes are poorly understood.

In this study, petrographically well-characterized hydrothermal rutile and other TiO<sub>2</sub> polymorphs were collected from highly mineralized porphyries and veins from Yulong for detailed analysis. The techniques used include: (1) scanning electron microscopy-backscattered electron (SEM-BSE) imaging and Raman spectroscopy for textural and mineralogical analysis; (2) electron microprobe analysis (EMPA) and mapping to quantify element abundances; and (3) in situ dating of hydrothermal rutile by laser ablation-inductively coupled plasma-mass spectrometry (LA-ICP-MS) to directly determine the U-Pb ages of hydrothermal activity and Cu-Mo mineralization. The data collected are then used to define the processes involved in the incorporation of trace elements, such as W, to gain a better insight into the evolution of hydrothermal systems that lead to a fertile porphyry deposit.

### GEOLOGICAL BACKGROUND

The Yulong deposit is situated in a 15–30 km wide and 300 km long zone containing porphyry Cu deposits. The zone is in the Qiangtang Terrane within the Himalayan-Tibetan Orogen (Tang and Luo 1995; Hou et al. 2003; Fig. 1a). The deposits are spatially and temporally associated with over 100 Eocene porphyry intrusions and K-rich mafic to felsic volcanic rocks. The intrusions are hosted by north to north-northwest (NNW) trending regional strike-slip faults, which are related to the culmination of the Paleocene to Eocene Eurasian-Indian continental collisional event (Hou et al. 2003; Yang et al. 2014; Wang et al. 2014, 2016, 2018a; Deng et al. 2017, 2018). The intrusions have LA-ICP-MS zircon U-Pb ages that decrease from ca. 44 Ma in the northwest to ca. 37 Ma ~100 km to the southeast (SE) (Liang et al. 2006; Fig. 1b).

The mineralized zone includes several medium, large, and giant Cu(-Mo-Au) deposits, which are interpreted as being associated with a post-subduction or post-collisional setting (Hou et al. 2015; Lu et al. 2015; Wang et al. 2018b). The Yulong deposit is the third largest porphyry-type Cu-Mo deposit in China, containing a resource of >1 Gt with an average grade of 0.62% Cu, 0.04% Mo, and 0.05 g/t Au (Yang and Cooke 2019). The deposit is hosted by the Yulong Granite, which is subdivided into a porphyritic monzogranite, with lesser amounts of porphyritic quartz monzonite, and rare dikes of porphyritic quartz gabbro recognized at depth (Fig. 1c; Tang and Luo 1995; Chang et al. 2017).

Intrusion of the Yulong Granite was structurally controlled by several ring-shaped, steeply dipping faults at the southern end of the north- to northwest-trending Hengxingcuo Anticline (Fig. 1c). The granite intrudes Triassic carbonate and clastic rocks and was emplaced at a depth of 1 to 3 km (Hou et al. 2003). The deposit is characterized by concentric alteration zones ranging from an inner K-silicate zone through a sericite and argillic zone to an outer propylitic zone. The highest Cu-Mo grades are present in the porphyritic monzogranite and faults around the pipe-like orebody (Figs. 1d–1e).

The porphyritic monzogranite hosts the majority of the Cu and Mo mineralization at the Yulong deposit (Figs. 2a–2b; Chang et al. 2017; Chen et al. 2021; Sun et al. 2021). The deposit includes

multiple stockwork veins, such as the early EB veins associated with biotite alteration (Fig. 2c), the A veins that consist of K-silicates (Fig. 2c), and the B veins that are associated with chlorite-sericite alteration selvages (Fig. 2d; Chen et al. 2021). Anatase and brookite polymorphs of TiO<sub>2</sub> found in the altered and mineralized porphyritic monzogranite form accessory minerals replacing altered titanite (Figs. 3b and 3c). In addition, a larger proportion of rutile is commonly present within or along the edge of medium- to high-temperature EB, A, and B quartz veins containing abundant sulfides. The occurrence of rutile in these veins shows that its genesis is closely related to the main stage of the Cu-Mo mineralization. Significantly, there is hardly any rutile in the late D veins formed at low temperatures.

### SAMPLING AND ANALYTICAL METHODS

#### Samples

Representative samples of core were collected from two diamond-drillholes and from depth in the Yulong mine. Eight thin and polished sections of rutile-bearing porphyritic monzogranite and hydrothermal veins were selected by microscopic examination for BSE, Raman, and EMPA analysis. Three rutile-bearing samples of hydrothermal veins were selected for U-Pb dating and trace element analysis by LA-ICP-MS. Detailed sample locations and descriptions are provided in Figure 1 and Online Materials<sup>1</sup> Table S1.

#### SEM-backscattered electron imaging

All the rutile grains analyzed in this study were from the polished 70 μm thick sections, which revealed the textural and genetic context of rutile associated with the Yulong Cu-Mo mineralization. The polished thin sections were coated with carbon for BSE imaging using a Tescan GAIA3 SEM-FIB equipped with an Oxford Instruments CL detector at the Beijing Research Institute of Uranium Geology (BRIUG), China. Images were acquired in BSE mode with an accelerating voltage of 15 keV and a primary beam current of 20 nA.

#### Raman spectroscopy

Raman spectra provide information on the mineral structures indistinguishable from microscopy and BSE imaging. The polymorphs of the Ti-oxide were confirmed using a LabRam HR800 Raman micro-spectrometer with a Zeiss microscope at the Institute of Geology and Geophysics, Chinese Academy of Sciences (IGGCAS), Beijing, China. The exciting radiation was provided by an argon ion laser with a wavelength of 532 nm and a source power of 44 mW. Phase identification used Raman wavenumbers at 143, 241, 443, and 612 cm<sup>-1</sup> for rutile; 144, 197, 400, 516, and 640 cm<sup>-1</sup> for anatase; and 153, 247, 322, and 636 cm<sup>-1</sup> for brookite (Meinhold 2010).

#### Electron microprobe analysis and elemental mapping

The major and minor element compositions of rutile and other minerals in polished sections were analyzed using a JEOL JXA-iHP200F EMPA at the Institute of Mineral Resources, Chinese Academy of Geological Sciences. For the analyses of biotite, magnetite, hematite and sericite, the accelerating voltage was 15 keV at a beam current of 20 nA, with beam spots of 1–10 μm. Counting times were 10–30 s on peak and half of this time on the respective backgrounds, depending on the element and mineral analyzed. Natural minerals and synthetic oxides were used as standards for calibration.

To obtain a lower detection limit for rutile crystals, the beam current and counting time were accordingly increased with analysis conditions of 15 keV accelerating voltage, 100 nA beam current, and 1 μm beam spot (Zack et al. 2004). The counting times for Si, Zr, Ti, Nb, Fe, Cr, Ta, W, and V are 90, 300, 15, 300, 150, 150, 300, 150, and 150 s, respectively, with respective detection limits of 23, 22, 253, 28, 49, 52, 29, 58 and 41 ppm. Natural andradite was used as a Si standard, natural rutile was used as a Ti standard, natural eskolaite was used as a Cr standard, synthetic magnetite was used for Fe, synthetic zircon was used as a Zr standard, and pure metals were used for W, Nb, and Ta standards. All mineral formulas were recalculated using the MINPET 2.0 software. High-sensitivity, low-resolution elemental mapping was carried out using similar analysis conditions as the spot analyses, and consumed ~4 h of instrument time for every sample.

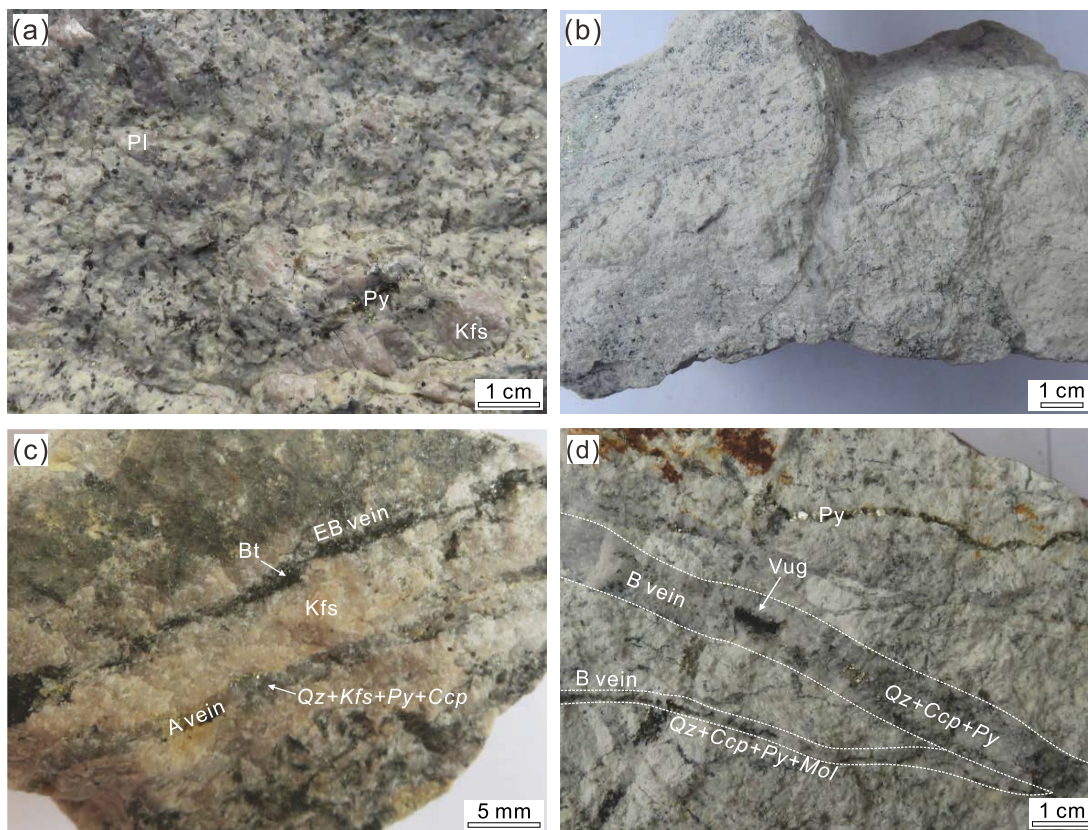


**FIGURE 2.** Hand specimen photographs of the syn-mineralization porphyritic monzogranite at Yulong showing: (a) porphyritic monzogranite; (b) argillic altered porphyritic monzogranite; (c) early (EB) biotite–quartz veins and quartz–K-feldspar–pyrite–chalcocopyrite (A) veins with potassic alteration; and (d) quartz–chalcocopyrite–pyrite (B) veins. Abbreviations: Pl = plagioclase; Kfs = K-feldspar; Py = pyrite; Qz = quartz; Bt = biotite; Ccp = chalcocopyrite; Mol = molybdenite. (Color online.)

### U-Pb dating and trace element analysis

Rutile U-Pb isotopic and trace-element measurements were carried out simultaneously using the LA-ICP-MS at the Nanjing Hongchuang Exploration Technology Service Co., Ltd. Radiometric data were obtained using a Wavelength Resonetics Resolution SE 193 nm Deep ultraviolet laser (Applied Spectra, U.S.A.) coupled to an Agilent 7900 (the U.S.A.) quadrupole ICP-MS. Pre-ablation was conducted for each spot analysis using 5 laser shots (~0.3  $\mu\text{m}$  in depth) to remove potential surface contamination. The analysis was performed using 30  $\mu\text{m}$  diameter spot at 5 Hz with fluence of 3  $\text{J}/\text{cm}^2$ . Analyses were conducted over 20 s background collection and 35–40 s ablation periods. The ablated material was carried by helium gas and subsequently mixed with argon prior to input into the plasma. Trace-element concentrations were determined using the rutile RMJG and NIST SRM 610 as a calibration standard and for correction of any instrumental drift, mass bias, and elemental fractionation. Measured masses included  $^{49}\text{Ti}$ ,  $^{27}\text{Al}$ ,  $^{28}\text{Si}$ ,  $^{51}\text{V}$ ,  $^{52}\text{Cr}$ ,  $^{56}\text{Fe}$ ,  $^{90}\text{Zr}$ ,  $^{93}\text{Nb}$ ,  $^{95}\text{Mo}$ ,  $^{118}\text{Sn}$ ,  $^{121}\text{Sb}$ ,  $^{178}\text{Hf}$ ,  $^{181}\text{Ta}$ ,  $^{182}\text{W}$ ,  $^{202}\text{Hg}$ ,  $^{204}\text{Pb}$ ,  $^{206}\text{Pb}$ ,  $^{207}\text{Pb}$ ,  $^{208}\text{Pb}$ ,  $^{232}\text{Th}$ , and  $^{238}\text{U}$  with a total sweep time of ~0.23 s. The internal standard was  $^{49}\text{Ti}$  with a content assumed as being stoichiometric. Every group of 10 spots on unknowns was bracketed by two analyses of the rutile RMJG standard ( $1758.4 \pm 9.7$  Ma,  $2\sigma$ ; Zhang et al. 2020) and two analyses of NIST SRM 610 glass standard. Reduction of both trace-element and U-Pb data was performed using the Iolite v2.5 software (Paton et al. 2011). The age calculations and plotting of concordia diagrams were completed using the ISOPLOT software (version 3.6; Ludwig 2008). Common lead uncorrected data were used to construct a Tera-Wasserburg plot to calculate the lower intercept and U-Pb age. The initial  $^{207}\text{Pb}/^{206}\text{Pb}$  common lead ratio was used for single spot age calculations (Williams 1998). Errors are quoted at the  $2\sigma$  (95% confidence) level and are propagated from all sources except mass spectrometer sensitivity and flux monitor. Full isotopic and trace-element data for the standards and samples are given in Online Materials<sup>1</sup> Table S3.

### RESULTS

#### Occurrence and texture

Rutile and other  $\text{TiO}_2$  polymorphs from Yulong, hydrothermal minerals in the altered porphyry and quartz veins, have variable textures and trace element compositions (see Table 1). All the analyzed  $\text{TiO}_2$  polymorphs are typically deep reddish-brown and subhedral to anhedral in shape, varying from below 20  $\mu\text{m}$

**► FIGURE 3.** Representative examples of photomicrographs (transmitted and reflected light) and BSE images of analyzed  $\text{TiO}_2$  polymorphs showing: (a–c) type-I brookite and anatase pseudomorphs after titanite in a fine-grained matrix of altered porphyry and contacting with monazite, chalcocopyrite, magnetite, and quartz; (d) elongated and prismatic type-II rutile in clusters associated with the alteration; (e and f) type-II rutile coexisting with relict titanite and showing faint zoning; (g–i) type-III rutile hosted by biotite and hematite showing patchy zoning; (j and k) irregular rutile coexisting with molybdenite; (l) anhedral and concentric zoning rutile intergrown with chalcocopyrite; (m and n) type-III rutile included in chalcocopyrite; and (o) patchy zoning of type-III rutile coexisting with pyrite. The circles and numbers represent the EMPA spots. Abbreviations: Ap = apatite; Ttn = titanite; Mag = magnetite; Kfs = K-feldspar; Rt = rutile; Ant = anatase; Brk = brookite; Hem = hematite; Py = pyrite; Qz = quartz; Bt = biotite; Ccp = chalcocopyrite; Mol = molybdenite; Cv = covellite. (Color online.) (See next page.)

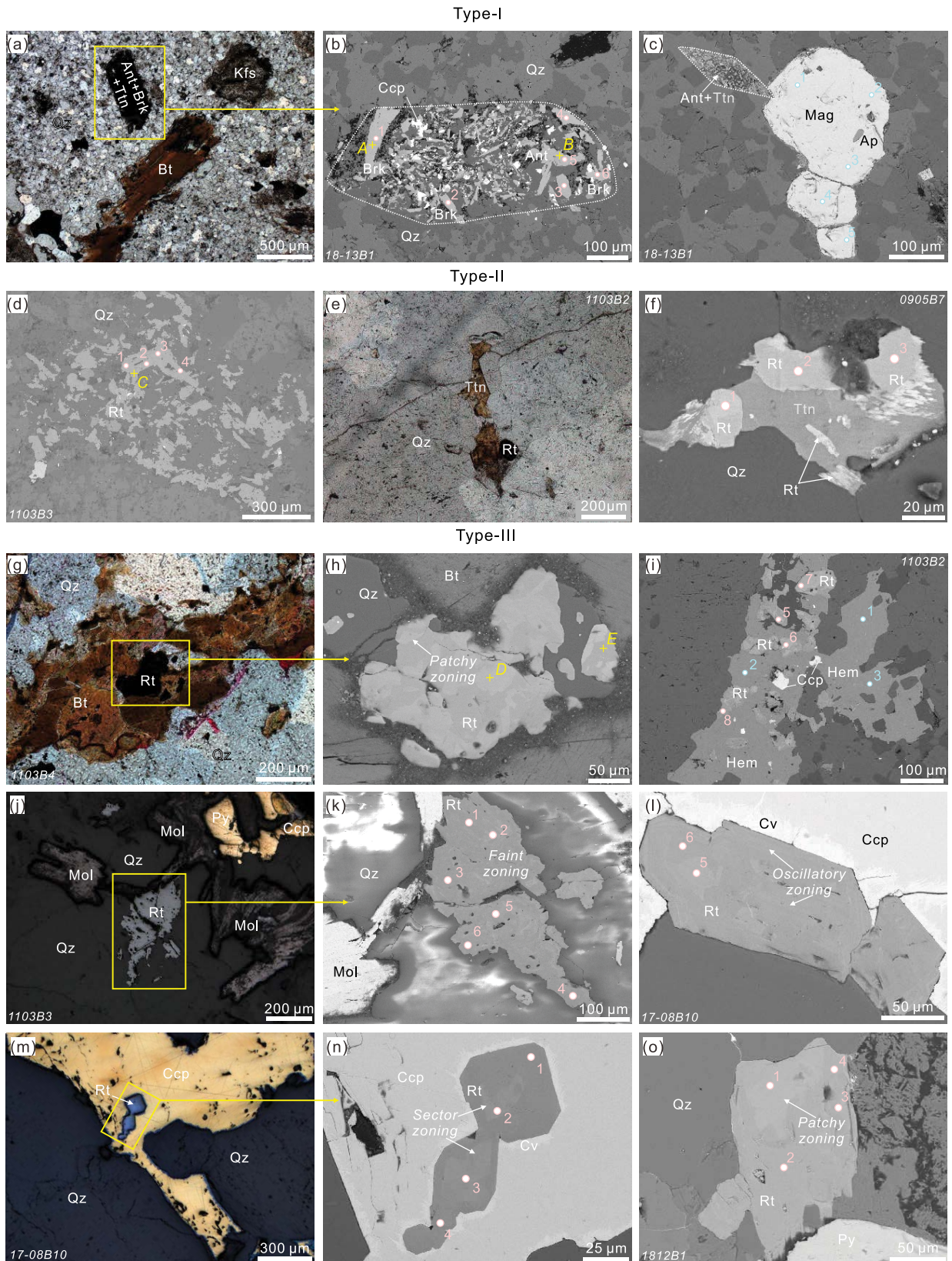


FIGURE 3.—SEE PREVIOUS PAGE.

**TABLE 1.** TiO<sub>2</sub> polymorphs textural features and assemblages in the Yulong Cu-Mo porphyry deposit

Types	Host rocks	Occurrence	Morphology	BSE texture
Type-I anatase and brookite	Fine-grained matrix of altered porphyritic monzogranite	Accessory hydrothermal altered mineral; pseudomorphic shape of titanite crystals contact with monazite, chalcopyrite, magnetite, and quartz	Subhedral and fine grains Size: 20–200 μm	Homogeneous
Type-II rutile	Hydrothermal veins or alteration envelope of altered porphyritic monzogranite	Occurs alone or in clusters in veins or alteration envelope; completely replacing titanite or coexisting with residual titanite	Anhedral, elongated, and prismatic grains Size: 50–300 μm	Faint zoning
Type-III rutile	Hydrothermal veins of altered porphyritic monzogranite	Hosted in biotite or hematite; intergrown with or included in pyrite, chalcopyrite and molybdenite	Anhedral, and irregular grains Size: 50–300 μm	Well-developed zoning patterns including oscillatory, patchy and sector zoning

to over 300 μm in diameter (Fig. 3). The three types of TiO<sub>2</sub> polymorphs identified based on their petrographic characteristics and mode of occurrence are: (1) the type-I TiO<sub>2</sub> minerals with the same micro-Raman spectra as brookite and anatase (Figs. 4a–4b), and (2) both the type-II and type-III composed of rutile crystals, but the Raman intensities are somewhat different at different positions (Figs. 4c–4d). For example, the intensity of ~442 cm<sup>-1</sup> wavenumber of W-rich rutile in type-III is significantly higher than that of W-poor rutile, and W-rich rutile has a peak at ~681 cm<sup>-1</sup> wavenumber.

The type-I brookite and anatase typically form pseudomorphs of titanite crystals in a fine-grained matrix of altered porphyry (Figs. 3a–3c). The titanite is not completely replaced by polymorphs that contain monazite and sporadic amounts of sulfides (e.g., chalcopyrite, Fig. 3b). The brookite and anatase are subhedral and fine grains display homogeneous BSE intensity (Figs. 3b and 3c).

The type-II rutile commonly forms elongated and prismatic grains, and appears alone in hydrothermal veins or in clusters

accompanying alteration envelopes (Figs. 3d and 3e). The rutile coexists with relict titanite and displays irregular and faint zoning on BSE images (Figs. 3d and 3f).

The type-III rutile is anhedral forming irregular grains in hydrothermal veins. Blocky rutile grains are hosted by biotite, sericite, and hematite, and are typically associated with the breakdown of Ti-rich minerals such as biotite and ilmenite (Figs. 3g–3i). Many rutile grains are also intergrown with or included in sulfides such as pyrite, chalcopyrite and molybdenite in B veins (Figs. 3j–3o). The type-III rutile displays well-developed zoning patterns including patchy, faint, oscillatory and sector zoning (Figs. 3h, 3k, 3l, and 3n), as found in other porphyry deposits, for example at El Teniente, Butte, and El Salvador (Rabbia et al. 2009; Mercer and Reed 2013; Schirra and Laurent 2021). Small rutile grains are intergrown with hydrothermal minerals such as zircon, apatite, and anhydrite in hydrothermal veins (Figs. 5a–5c), but are rarely associated with magnetite (Fig. 5d).

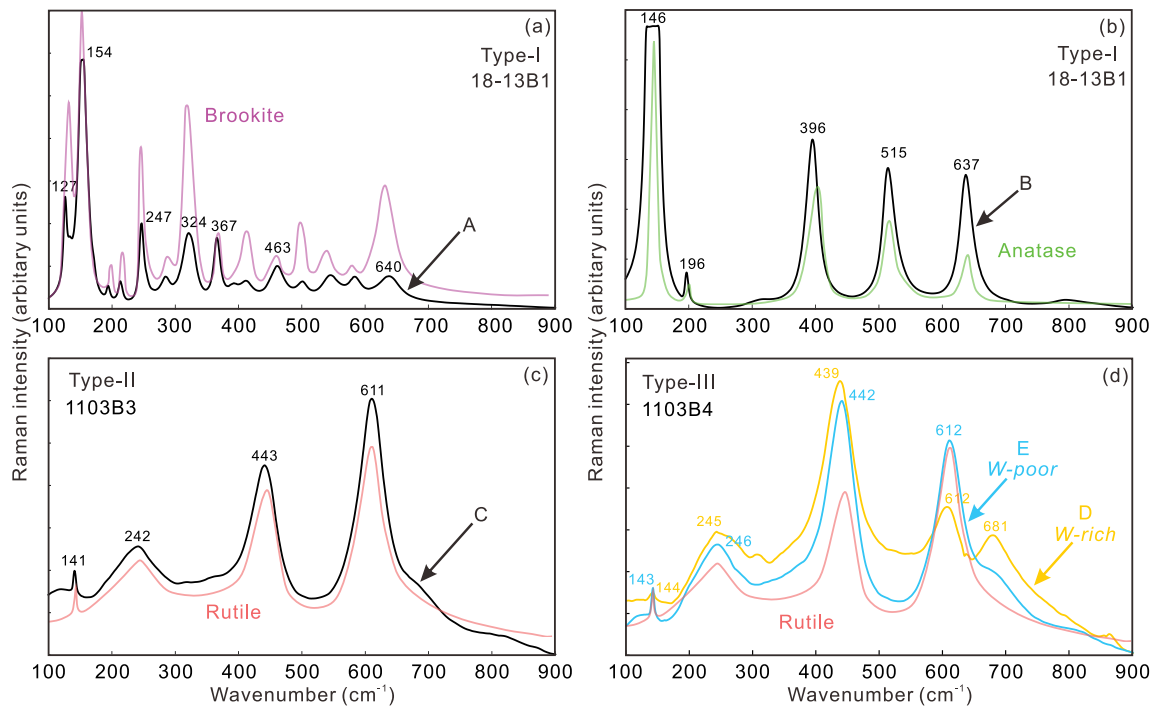


**FIGURE 4.** Comparison of Raman spectra between the standard TiO<sub>2</sub> polymorphs (brookite, anatase, and rutile; Meinhold 2010) from Yulong showing: (a–b) type-I brookite and anatase from sample 18-13B1; (c) type-II rutile from 1103B3; and (d) type-III rutile from 1103B4. The spots at which the Raman spectra were collected are marked with letters and crosses in Figure 3. (Color online.)

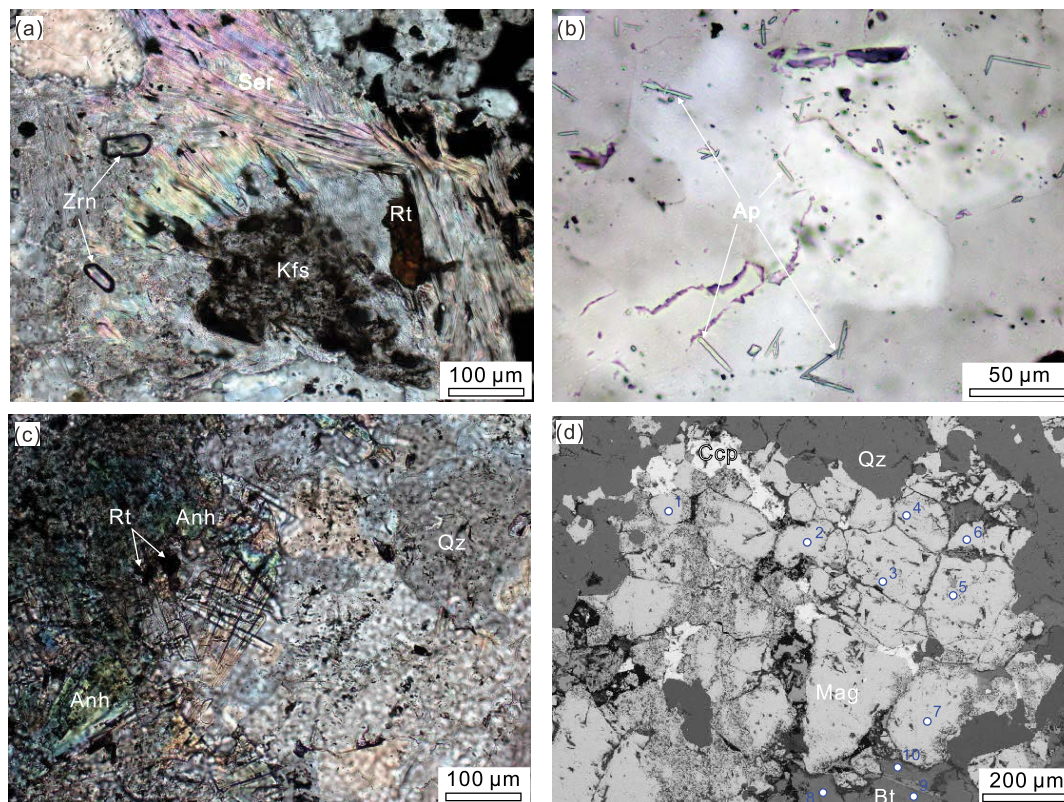


**FIGURE 5.** Representative photomicrographs in transmitted light and BSE images showing: (a) rutile associated with quartz, K-feldspar, zircon, and sericite in veins; (b) columnar apatite inclusions widely distributed in veins; (c) rutile coexisting with anhydrite in the vein halo; and (d) magnetite in EB veins. Abbreviations: Qz = quartz; Rt = rutile; Kfs = K-feldspar; Zrn = zircon; Ser = sericite; Mag = magnetite; Anh = anhydrite; Ap = apatite; Bt = biotite. (Color online.)

### Major and minor element composition

In situ chemical analyses of rutile carried out using EMPA are shown in Figure 6 and summarized in Online Materials<sup>1</sup> Table S2. Concentrations of most trace elements are heterogeneous within each sample and each type. The type-I brookite and anatase in the porphyritic monzogranite contain high-Si (up to 0.89 wt%) and -Zr (up to 0.28 wt%) contents, but low-Cr (<0.05 wt%), -Ta (<0.05 wt%), and -W (<0.01 wt%) contents. The type-II rutile has a similar range of Fe and Ta contents as the type-I brookite and anatase, but slightly higher V, Cr, and W contents. The type-III rutile in veins contain significantly variable Fe (0.39–3.51 wt%), V (0.84–1.80 wt%), Nb (0.07–4.89 wt%), and W (0.12–7.11 wt%) contents, but low-Zr (<0.07 wt%), -Si (<0.11 wt%), -Cr (<0.52 wt%), and -Ta (<0.14 wt%) contents. Compared with the type-II rutile, the type-III rutile has significantly higher V and W, and more variable Fe contents (Online Materials<sup>1</sup> Table S2). For the purpose of comparison, the type-III rutile is subdivided into W-rich and W-poor rutile.

The three types of rutile at Yulong show a negative correlation between W and Ti (Fig. 6a), whereas the V contents only display an obvious negative correlation with Ti in the type-III W-rich rutile (Fig. 6b). In addition, the type-II rutile has a more variable Nb content, and the concentrations of V and Nb cannot be correlated (Fig. 6c). The W and V contents of the other type-II and type-III rutile appear to be positively correlated

(Fig. 6d). The V contents of all the types of rutile increase with increasing W contents. The W-rich type-III rutile has higher V and Fe contents, but lower Nb contents than type-II and W-poor type-III rutile grains (Fig. 6e). In addition, the type-I data cluster in the  $2\sigma$  field for brookite, and most of the data from the type-II and -III grains cluster in the  $2\sigma$  field for rutile (Fig. 6f) from Triebold et al. (2011).

The EMPA mapping indicates that the elements are unequally distributed in the apparent homogeneous, faint, or patchily zoned type-II and III rutile grains (Fig. 7). High concentrations of trace elements are displayed on the EMPA images as warm colors (red, yellow, green) and the low concentrations appear as cool colors and tones (blue, purple, black). For example, the bright zones in the BSE images of the rutile grains interlocking with biotite contain more W than darker zones, and patches with variable bright zones locally show elevated V and Nb values (Fig. 7b). Similar element mapping results are also found in rutile intergrown with other minerals (Online Materials<sup>1</sup> Figs. A1–A2).

Biotite, magnetite, and other alteration minerals associated with rutile were scanned with the EMPA (Online Materials<sup>1</sup> Table S2). The results show that the TiO<sub>2</sub> content of magnetite in ore-bearing porphyry and quartz (EB) veins is generally low (<0.24 wt%). In contrast, the hydrothermal biotite is enriched in Ti (1.16–2.68 wt% TiO<sub>2</sub>). The Ti content of sericite and hematite in hydrothermal alteration zones is also generally low (<0.4 wt%).

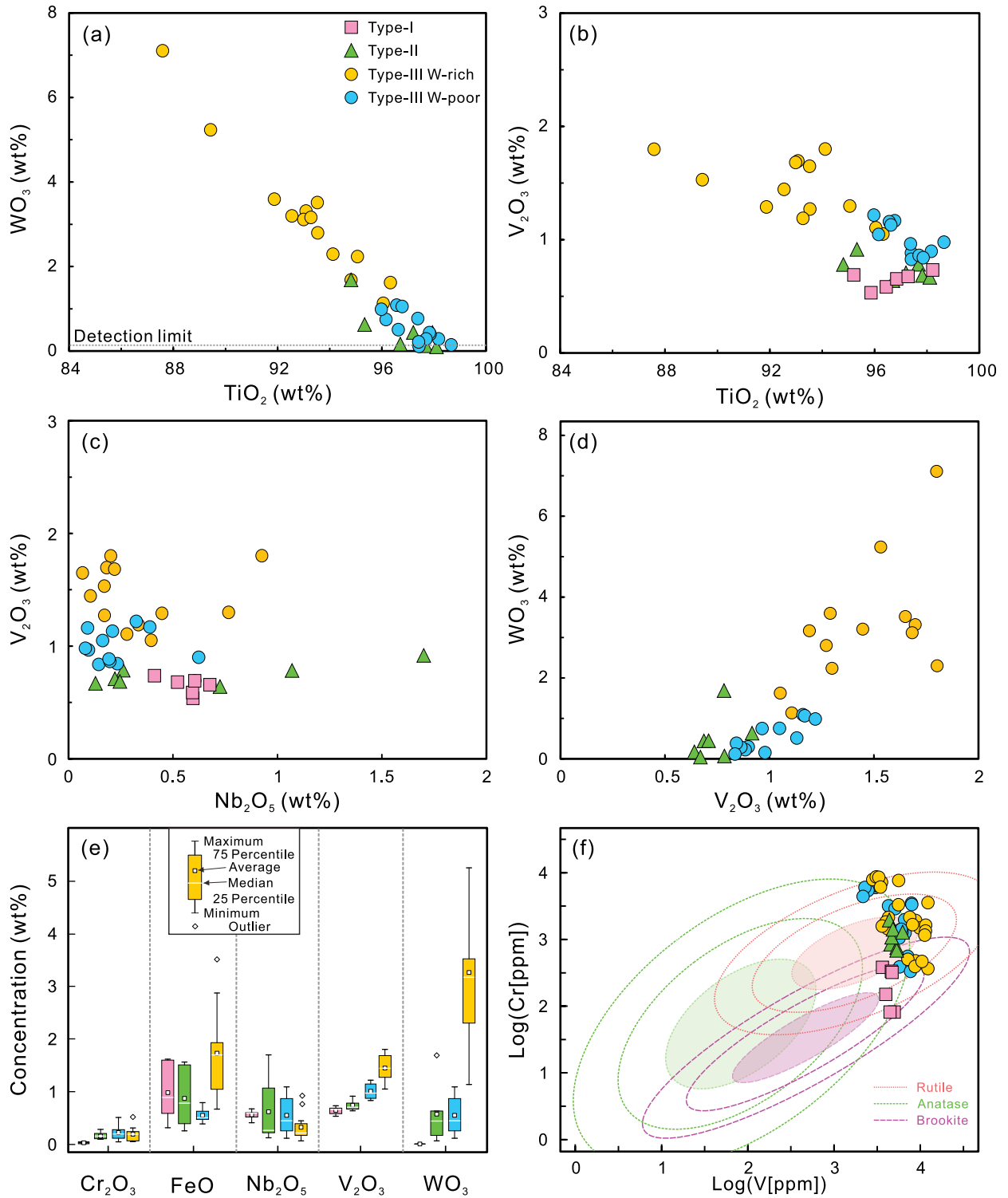


**FIGURE 6.** Concentrations of selected oxides and trace elements in TiO<sub>2</sub> polymorphs showing: (a) TiO<sub>2</sub> vs. WO<sub>3</sub>; (b) TiO<sub>2</sub> vs. V<sub>2</sub>O<sub>3</sub>; (c) Nb<sub>2</sub>O<sub>5</sub> vs. V<sub>2</sub>O<sub>3</sub>; (d) V<sub>2</sub>O<sub>3</sub> vs. WO<sub>3</sub>; (e) box-and-whisker diagram (constructed from spot EMPA images) for oxide concentrations; and (f) V vs. Cr plot with 1-, 2-, and 3-σ probability regions for rutile, anatase, and brookite (modified after Triebold et al. 2011). (Color online.)

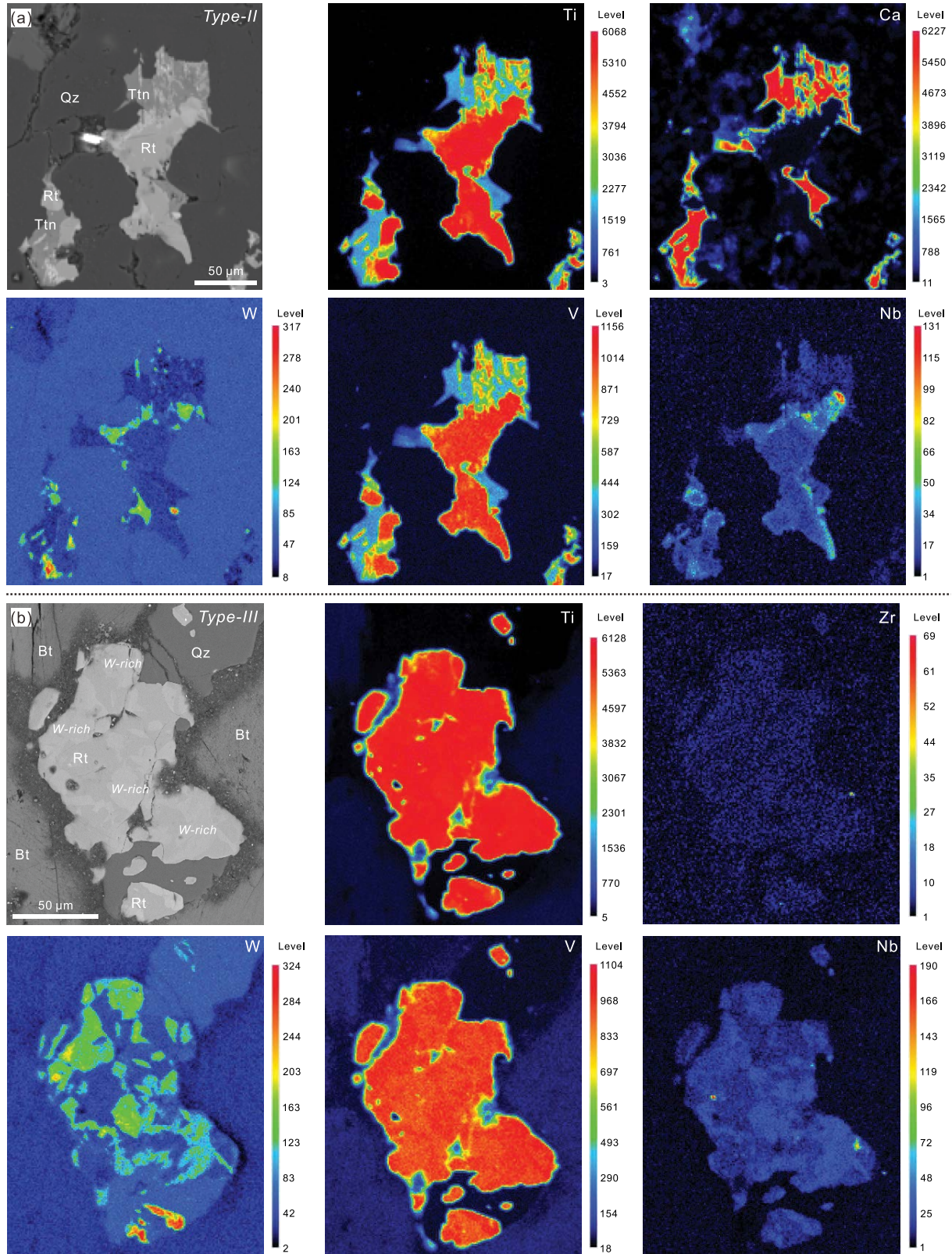


**FIGURE 7.** EMPA trace element mapping of: (a) type-II rutile; and (b) type-III rutile. The vertical scale represents the EMPA counts per unit area. The high concentrations of trace elements are shown in red, yellow, and green, and the low concentrations are shown in blue, violet, and dark colors. Abbreviations are the same as Figure 3. (Color online.)

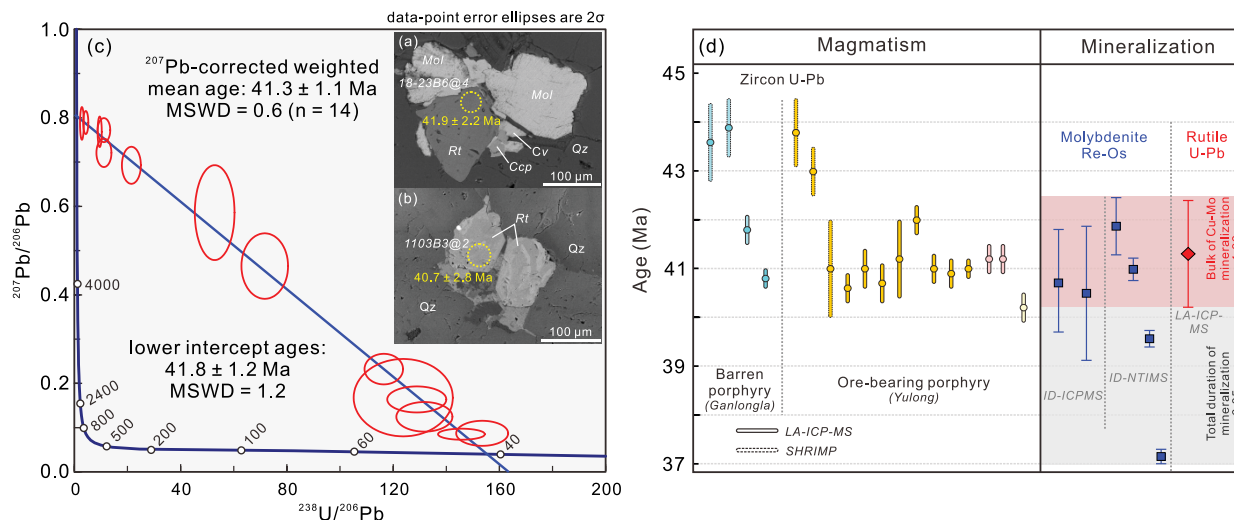


**FIGURE 8.** (a–b, inset in c) BSE images of two representative rutile grains from the Yulong deposit showing the LA-ICP-MS analysis spots and results; (c) LA-ICP-MS rutile U-Pb Tera-Wasserburg diagram for type-III rutile in hydrothermal veins; and (d) the summary of the zircon U-Pb, molybdenite Re-Os, and rutile U-Pb (this study) data for the Yulong porphyry Cu-Mo deposit (data sources: Chen et al. 2021 and references therein). (Color online.)

### LA-ICP-MS U-Pb dating

Seventeen U-Pb isotopic analyses were completed on vein-hosted type-III rutile (samples 18-23B6, 1103B3, and 17-08B10). Results of U-Pb dating and concordia diagrams are presented in Figure 8 and Online Materials<sup>1</sup> Table S3. The rutile analyzed in this study has variable U contents (10.5–173 ppm) and variable percentages of radiogenic  $^{206}\text{Pb}$ , but a generally high proportion of common lead as reflected by the spread of the discordant data points. Three analyses were disregarded owing to high concentrations of common Pb, low U, and the presence of Si-rich inclusions. On the Tera-Wasserburg plot, linear regression of the uncorrected data of 14 analyses yields a lower intercept age of  $41.8 \pm 1.2$  Ma ( $2\sigma$ , MSWD = 1.2) with an initial  $^{207}\text{Pb}/^{206}\text{Pb}$  ratio of  $0.8059 \pm 0.015$  (Figs. 8a–8c), which was used to calculate individual spot ages that yielded a weighted average  $^{206}\text{Pb}/^{238}\text{U}$  age of  $41.3 \pm 1.1$  Ma ( $2\sigma$ , MSWD = 0.6, Fig. 8c).

## DISCUSSION

### Rutile U-Pb geochronology related to Cu-Mo mineralization

Prior studies have constrained the timing of magmatism and Cu-Mo mineralization at the Yulong deposit (Tang and Luo 1995; Hou et al. 2003; Chen et al. 2021 and references therein). The ages of the ore-bearing porphyry have been constrained within a ca. 3.6 Ma time span bracketed by U-Pb zircon LA-ICP-MS/SHRIMP dating from the earliest porphyritic monzogranite dated at  $43.8 \pm 0.7$  Ma (Wang et al. 2009) to the porphyritic quartz gabbro dated at  $40.2 \pm 0.3$  Ma (Chang et al. 2017). The barren porphyritic monzonite at Ganlongla over 1 km to the north is coeval with the ore-bearing porphyritic monzogranite (Figs. 1a and 8d). Previous ID-ICP-MS and recent high-precision ID-NTIMS Re-Os molybdenite dating show that the deposit was mineralized over a period of ~5.1 million years (Hou et al. 2006; Chang et al. 2017). The bulk of the Cu-Mo mineralization,

therefore, developed in a period of ca. 1.4 million years from the early-stage  $A_{2E}$  veins dated at  $42.3 \pm 0.2$  Ma to transitional stage  $B_T$  veins dated at  $40.9 \pm 0.2$  Ma (Fig. 8d; Chang et al. 2017). Furthermore, the high-precision Re-Os molybdenite age of ca. 41 Ma does not bracket the complete age of the mineralizing event (Fig. 8d; Chiaradia et al. 2014; Schirra and Laurent 2021).

Most rutile crystals at the Yulong deposit formed broadly synchronously with hydrothermal quartz, biotite, and most of the sulfides in the potassic and phyllic alteration zones. This means the rutile will record the age of porphyry mineralization. An advantage of LA-ICP-MS rutile U-Pb dating is that it typically contains adequate U and radiogenic Pb for accurate dating (Santos et al. 2020; Schirra and Laurent 2021). The closure temperature for Pb diffusion in rutile is strongly dependent on the grain size. For a cooling rate of  $1 \text{ }^\circ\text{C Ma}^{-1}$  and spherical geometry, Cherniak (2000) determined closure temperature ( $T_c$ ) values of  $567 \text{ }^\circ\text{C}$  for  $70 \text{ }\mu\text{m}$  size grains and  $617 \text{ }^\circ\text{C}$  for  $200 \text{ }\mu\text{m}$  size grains. This  $T_c$  is higher than the formation temperature of hydrothermal quartz veins reflected by the homogenization temperatures ( $T_h$ ) of fluid inclusions [ $\sim 500$ – $600 \text{ }^\circ\text{C}$  in the EB and A veins, and  $\sim 375$ – $500 \text{ }^\circ\text{C}$  in the B veins (Sun et al. 2021)]. Consequently, rutile fulfills the basic requirements for a reliable U-Pb geochronometer. The U-Pb dating of hydrothermal rutile should yield the crystallization ages and the timing of given hydrothermal mineralization, instead of representing cooling ages.

In this study, in situ U-Pb dating of the rutile yields a lower intercept age of  $41.8 \pm 1.2$  Ma (Fig. 8c), which overlaps with the previously reported molybdenite Re-Os ages (Fig. 8d). Significant scatter and abnormal MSWD values of the rutile U-Pb data within a single sample could be due to multiple preserved generations of rutile (Figs. 8a–8b). Furthermore, the common Pb incorporation in rutile grains could also result in over-dispersion without a requirement for multiple rutile populations (e.g., Plavska et al. 2018; Santos et al. 2020). This could be accounted for by U-Pb perturbation during dissolution and reprecipitation above

the  $T_c$  for rutile in the early hydrothermal process. Although the internal precision of individual rutile U-Pb weighted mean dates is significantly lower than that of the zircon U-Pb and molybdenite Re-Os, they all overlap within the uncertainty and are not resolvable. This suggests that the bulk of the Yulong Cu-Mo mineralization formed broadly synchronously with the emplacement of the porphyritic monzogranite.

### Origin and formation environment of TiO<sub>2</sub> polymorphs

The distinctive textures and compositions of TiO<sub>2</sub> polymorphs replacing Ti-rich minerals during hydrothermal alteration in porphyry Cu(-Mo-Au) deposits may better reflect the mineralization processes. TiO<sub>2</sub> polymorphs in the fine-grained matrix and hydrothermal veins studied coexist with typical hydrothermal biotite, anhydrite, sericite, magnetite, and sulfides (e.g., chalcopyrite, molybdenite, and pyrite), indicating a hydrothermal origin (Fig. 3). Likewise, these polymorphs can reflect different temperature and pressure conditions, driven by hydrothermal fluids (Triebold et al. 2011; Plavsa et al. 2018).

Anatase and brookite typically form during low temperature and pressure metamorphism and alteration, with aqueous low- $T$  conditions promoting their stability (Smith et al. 2009; Plavsa et al. 2018). The type-I brookite and anatase at Yulong are present in a fine-grained matrix of altered porphyry and commonly pseudomorph magmatic titanite (Figs. 3a–3c). This highlights the role of low-temperature hydrothermal fluids in destabilizing primary Ti-bearing minerals during argillic alteration. This interpretation is also confirmed by porphyry hand specimens that are overprinted by strong argillic alteration in the late-stage mineralization (Fig. 2b). Lower temperature polymorphs (anatase and brookite) have geochemical signatures systematically different from those of rutile. Previous studies have demonstrated that the availability of HFSE and base metals such as V-Cr-W-Fe for inclusions in the brookite and anatase is largely controlled by the breakdown of precursor Ti-rich minerals and co-precipitation of other phases (Triebold et al. 2011; Plavsa et al. 2018).

Rutile associated with porphyry copper deposits forms at temperatures between ~400 and 700 °C, pressures of a few hundred MPa,  $f_{O_2}$  above the nickel-nickel oxide (NNO) buffer, and under hydrous conditions (Rabbia and Hernández 2012). A hydrothermal fluid associated with the overall development of a porphyry deposit does not have a consistent temperature,  $f_{O_2}$ , pH, and chlorine content, and such fluids interact with the ore-bearing porphyry (Rabbia and Hernández 2012). The presence of rutile crystallizing during hydrothermal alteration can be interpreted as representing localized re-equilibration and breakdown of Ti-rich minerals, such as titanite, biotite, and ilmenite (Scott 2005; Rabbia et al. 2009).

The chemical stability of pre-existing Ti-rich minerals is extremely susceptible to high-temperature and SO<sub>2</sub>-rich oxidizing fluids, which could explain why rutile is present in zones of hydrothermal alteration in porphyry deposits (Rabbia and Hernández 2012). Fluids metasomatism promoted the incomplete replacement of the earlier titanite by type-II rutile in the early hydrothermal quartz A veins (e.g., titanite + SO<sub>2</sub>-rich fluid → anhydrite + quartz + rutile), which also records the breakdown of Ti-rich minerals during the introduction of high-temperature fluids (Figs. 3d–3f).

In contrast to titanite and ilmenite, Ti-rich magmatic biotite and hornblende initially re-equilibrate to hydrothermal biotite during K-alteration (e.g., Rabbia and Hernández 2012; Mercer and Reed 2013; Xiao et al. 2021). The breakdown of Ti-rich biotite is regarded as the main mechanism generating hydrothermal rutile associated with veins developed during widespread K-alteration in the Yulong deposit (Figs. 3g–3h). Under a subsequent moderate temperature of 300–400 °C, at elevated  $f_{O_2}$  levels during phyllic alteration, hydrothermal magnetite becomes unstable and is completely replaced by hematite intergrown with hydrothermal rutile (Fig. 3i). The relatively high Ti concentration (1.16–2.68 wt%) of hydrothermal biotite at Yulong makes it a potential source for rutile. Additionally, the intergrowth relationships between individual, blocky type-III rutile and Cu-Fe sulfides in hydrothermal veins (i.e., B veins; Figs. 3j–3o) support the conclusion that rutile is a product of precipitation from aqueous fluids as a vein-filling phase indicative of Ti migration. A similar relationship of rutile forming synchronously with Cu-Mo mineralization has been reported for deposits such as Batu Hijau, Bingham Canyon, El Salvador, and North Parkes (Schirra and Laurent 2021).

The composition of hydrothermal fluid is another factor controlling the growth of rutile (Rabbia and Hernández 2012; Schirra and Laurent 2021). Recent experimental work on high-temperature metamorphic rocks demonstrates that the solubility of rutile increases significantly in F- and Cl-rich brines (Rapp et al. 2010). Apatite is known to preferentially incorporate F, and apatite inclusions are widely recognized in various stages of hydrothermal veins at Yulong (Fig. 5b; Chang et al. 2018). Once the precipitation of apatite took place, the mineralizing fluids became depleted in F, consequently reducing the solubility of Ti, Zr, and other HFSE resulting in Ti saturation and the crystallization of rutile. In addition, unlike the slow heating and cooling processes in metamorphic rocks, hydrothermal rutile is commonly formed in events with rapid pulsating fluid flow leading to the enrichment of Zr (Cabral et al. 2015; Agangi et al. 2019; Feng et al. 2020). The estimated rutile crystallization temperature in this study using the Zr-in-rutile thermometer of Tomkins et al. (2007) is over 100 °C higher than the fluid inclusion temperature reported by Sun et al. (2021), demonstrating that Zr-in-rutile thermometer is not appropriate for use in rutile of hydrothermal origin (Cabral et al. 2015). Thus, the origin of rutile in hydrothermal veins might be due to the effect of fluorine (i.e., fluorapatite) on the solubility of rutile.

### Introduction of W in the hydrothermal rutile

The composition of hydrothermal rutile in this study has wide variations in the concentrations of Fe, Cr, W, and V (Fig. 9). Consequently, a single-spot analysis may not be representative of the bulk composition of rutile grains, similar to what was seen by Meinhold (2010). Combining BSE images with elemental mapping of rutile grains can reveal complex zonation patterns or patchy zoned crystals. Our analyses of rutile crystals show that W content correlates positively with BSE brightness (Figs. 7 and 10), and the patchy or sector zonation is controlled by the distribution of trace elements in rutile.

The crystal structure of rutile consists of chains of TiO<sub>6</sub><sup>2-</sup> octahedra that link each oxygen in triangular coordination with Ti<sup>4+</sup>

**FIGURE 9.** Selected trace element compositions of rutile from Yulong deposit. The background shades indicate the compositional ranges of rutile from metamorphic, igneous and sedimentary environments, and other porphyry deposits reported in the literature (Data sources: Luvizotto and Zack 2009; Meyer et al. 2011; Okay et al. 2011; Ewing et al. 2013; Gao et al. 2014; Şengün and Zack 2016; Hart et al. 2018; Plavsa et al. 2018; Ver Hoeve et al. 2018; Rösel et al. 2019; Pereira et al. 2019; Pe-Piper et al. 2019; Agangi et al. 2020; Şengün et al. 2020; Schirra and Laurent 2021). (Color online.)

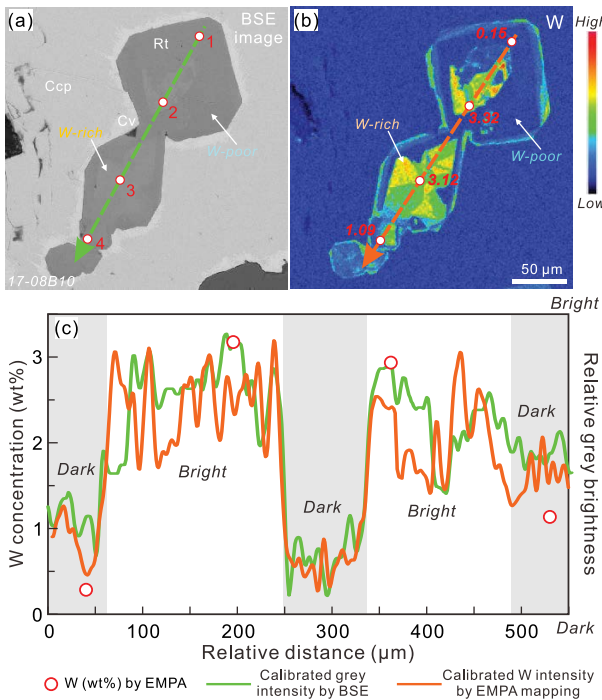
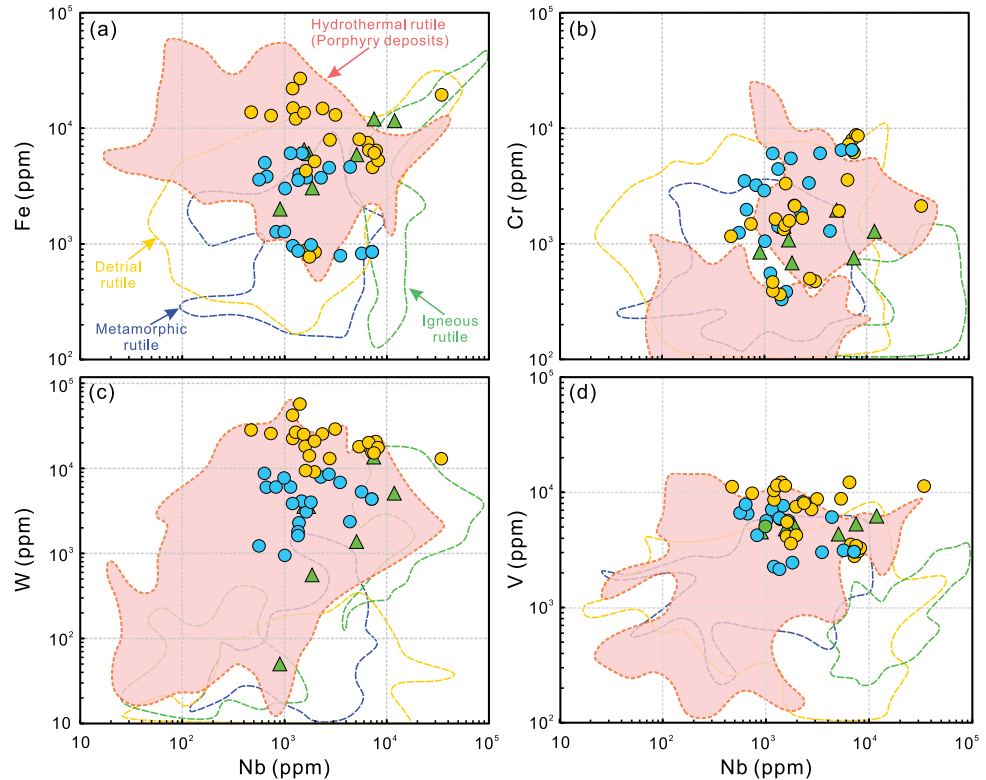


**FIGURE 10.** Relationship between W concentrations and BSE intensity. The arrows show examples of traverses across rutile with different W concentrations. The original W intensity profiles by EMPA mapping are shown in orange curves, smoothed BSE intensity profiles are shown in green curves, and EMPA spots are shown with circles. (Color online.)

ions (Baur 2007; Klein and Dutrow 2007). It has been found in previous studies that Ti in the rutile structure can be substituted by W, Fe, V, and Nb, and the substitution of  $Ti^{4+}$  is controlled by the ionic radius and ionic charge of the substituted cation (Meinhold 2010; Win et al. 2017; Reznitsky et al. 2017; Agangi et al. 2019, 2020; Adlakha et al. 2020).

The oxidation state of Fe, V, Nb, Cr, and W in rutile of this study and their substitution mechanisms are evaluated using binary plots (Fig. 11). The cation percentages were calculated using the number of total cations for oxygen being 2, and iron predominantly being incorporated into rutile as  $Fe^{3+}$  (Murad et al. 1995; Bromiley et al. 2004; Win et al. 2017). The  $M^{3+}$  represents the trivalent cations (i.e.,  $Fe^{3+}$ ,  $Cr^{3+}$ , and  $V^{3+}$ ). The slope of Ti and V range from  $-1$  to  $-1/3$ , reflecting the equation  $V^{3+} + M^{5+} \leftrightarrow 2Ti^{4+}$  in the W-poor rutile and  $2V^{3+} + W^{6+} \leftrightarrow 3Ti^{4+}$  in the W-rich rutile, but the direct substitution of  $V^{4+}$  for  $Ti^{4+}$  is rare (Fig. 11a). The partial trivalent elements Fe, Cr, and V for the W-poor rutile, and the Nb content of rutile containing  $M^{3+}$  exhibit a slope  $>1$  (Fig. 11b), reflecting the compatibility of different valences (i.e.,  $V^{5+}$ , or  $Fe^{2+}$ ) in rutile. The correlation between the  $M^{3+}$  and  $W^{6+}$  in the W-rich rutile corresponds to a slope of 2 (Fig. 11c), indicating coupled substitutions with a strong correlation following the chemical equation  $2M^{3+} + W^{6+} \leftrightarrow 3Ti^{4+}$ . The correlation between W and Fe in the W-rich rutile (slope = 2; Fig. 11d), is consistent with the Equation  $2Fe^{3+} + W^{6+} \leftrightarrow 3Ti^{4+}$ . A strong negative correlation between Ti and  $W^{6+} + 2M^{3+}$  in the W-rich rutile grains (slope =  $-1.02$ ,  $R^2 = 0.98$ ) clearly shows that W incorporated into the hydrothermal rutile is largely controlled by the reaction  $2M^{3+} + W^{6+} \leftrightarrow 3Ti^{4+}$  (Fig. 11e). Based on the correlations between Ti and  $Nb^{5+} + 2M^{3+}$  of the W-poor

rutile (slope =  $-1.03$ ,  $R^2 = 0.88$ ; Fig. 11f),  $\text{Nb}^{5+}$  might substitute into the rutile structure following the similar reaction  $\text{M}^{3+} + \text{Nb}^{5+} \leftrightarrow 2\text{Ti}^{4+}$ . In addition, many rutile grains contain high concentrations of Fe, Cr, and V relative to Nb or W, as the data trends plot above the correlation line without intersecting 0 (Figs. 11a and 11c). This is explained by excess amounts of  $\text{Fe}^{3+}$ ,  $\text{Cr}^{3+}$ , and  $\text{V}^{4+}$  substituting for  $\text{Ti}^{4+}$  in rutile.

Alternatively, the possibility of vacancy-bearing substitutions has been proposed, with hydrogen atoms or OH groups being involved in local charge compensation at the oxygen position in rutile and cassiterite samples (Maldener et al. 2001; Losos and

Beran 2004; Borges et al. 2015). However, recent Raman and X-ray absorption spectroscopy studies of W-rich rutile exclude the possibility of hydrogen acting as a charge-balancing species or oxygen vacancies (Majzlan et al. 2021). These suppositions are also not supported by analyses completed in this study.

Another parameter that favors the substitution of Ti by W is the similarity in their ionic radii (Shannon 1976). Under the condition of charge balance, the virtually identical ionic radius in sixfold coordination of  $\text{W}^{6+}$  (0.74 Å) is arguably favorable for the replacement of  $\text{Ti}^{4+}$  (0.745 Å) in the rutile structure. In addition to these mechanisms, non-equilibrium incorporation of

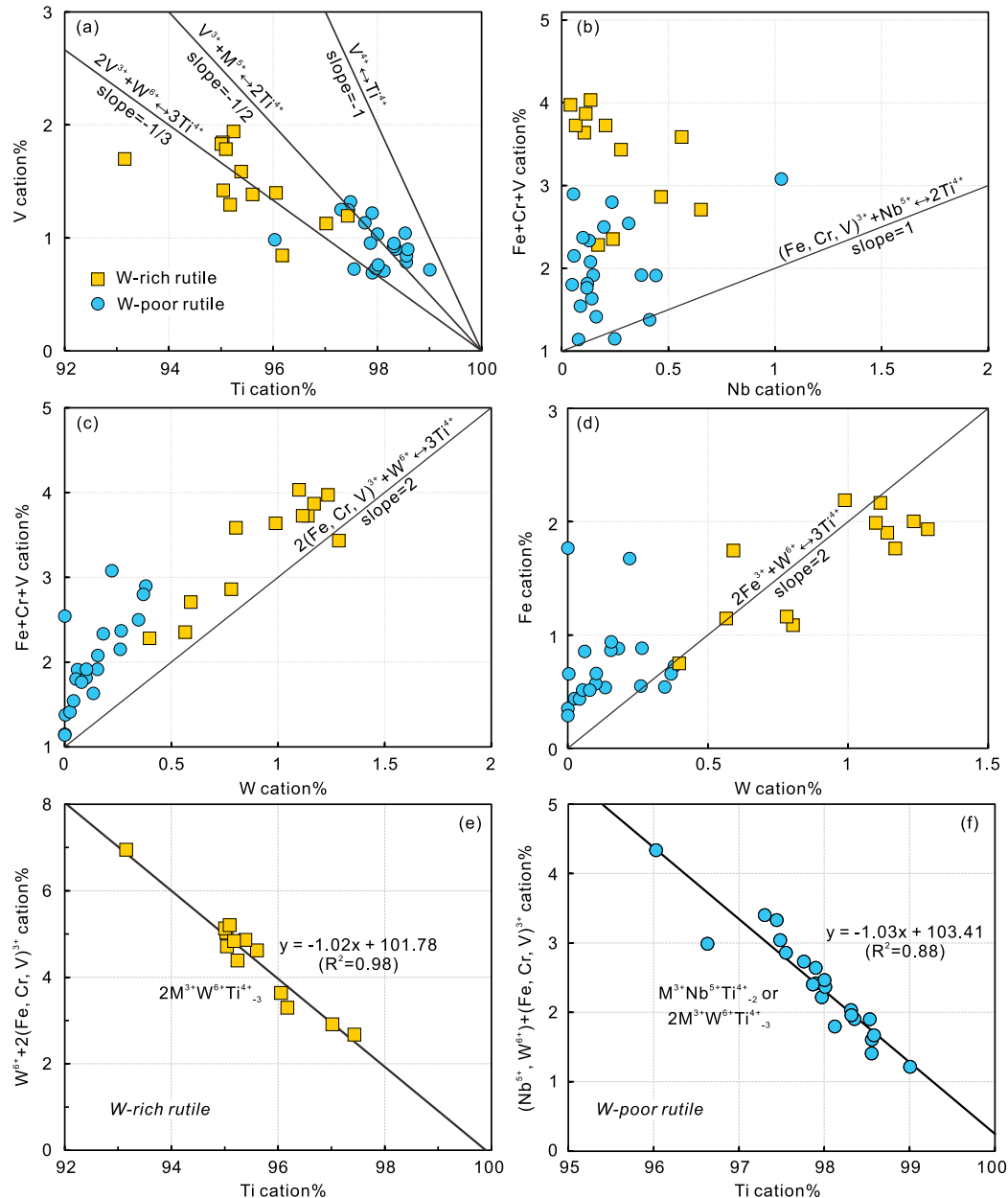


**FIGURE 11.** Binary plots of element abundances in rutile using EPMA data recalculated as atomic cation percent: (a) Ti and V; (b) Nb and Fe+Cr+V; (c) W and Fe+Cr+V; (d) W and Fe; (e) Ti and  $\text{W}^{6+}+2(\text{Fe, Cr, V})^{3+}$ ; and (f) Ti and  $(\text{Nb}^{5+}, \text{W}^{6+})+2(\text{Fe, Cr, V})^{3+}$ . Trendlines rooted are shown representing different substitution mechanisms, and  $\text{M}^{3+}$  indicates the sum of the trivalent elements. (Color online.)

trace elements during fast mineral growth in hydrothermal ore systems (Agangi et al. 2019) cannot be ignored.

### Source of W and hydrothermal fluid signatures in the Yulong porphyry Cu-Mo deposit

Previous studies show that the presence of pathfinder elements such as W, Nb, V, Sn, and Fe in hydrothermal rutile is influenced by the nature of precursor minerals and the composition of magmatic or metamorphic fluids (Plavsa et al. 2018; Agangi et al. 2020; Schirra and Laurent 2021). Rutile at Yulong contains high levels of W, V, Fe, and Cr (Fig. 9), similar to rutile from other porphyry deposits (Scott 2005; Rabbia et al. 2009; Mercer and Reed 2013; Schirra and Laurent 2021). We, therefore, interpret the chemical composition of rutile formed in a hydrothermal ore system to reflect the composition of ore-forming fluids associated with porphyry Cu-Mo mineralization.

The crystallographic control of impurities into the rutile lattice during crystal growth can cause compositional variations such as sector zoning (Plavsa et al. 2018; Agangi et al. 2020; Moore et al. 2020; Majzlan et al. 2021). The intensity of back-scattered luminescence is related to the relative atomic mass of elements. Due to the common presence of elements such as W, Nb, V, and Fe heavier than Ti, the incorporation of trace elements results in brighter sectors in BSE images. In this study, hydrothermal rutile preserves well-developed patchy and sector zoning (Figs. 10a–10b), which largely relates to the contribution of W (Fig. 9c). However, the elemental mapping of residual titanite that is incompletely replaced by rutile in the quartz veins shows extremely low-W content (Fig. 7a), indicating that W is unlikely inherited from primary Ti-rich minerals. In general, several HFSEs, such as W, Nb, and V, form complexes with F in aqueous fluids. These elements tend to be enriched in rocks formed from strongly fractionated, typically F-rich and high-Cl felsic magmatic-hydrothermal fluids (Carruzzo et al. 2006; Chevychev et al. 2005; Agangi et al. 2020). The presence of F-bearing phases in the minerals studied, such as fluorapatite (e.g., average 3.13 wt% F; Huang et al. 2019), indicates the presence of F in the mineralizing fluids, explaining the mobilization of HFSEs (Fig. 12). The latest studies of the composition of fluid inclu-

sions, using LA-ICP-MS, confirm that brine and intermediate density inclusions in the early- and transitional-stage quartz veins represent the main mineralization event at Yulong. The inclusions contain W assaying up to thousands of parts per million (Chang et al. 2018). Furthermore, the presence of high-valence cations also points toward high  $f_{O_2}$  during the hydrothermal alteration in the porphyritic monzogranite at Yulong, which is further supported by the presence of texturally associated anhydrite (Fig. 5c).

Deciphering the signatures of ore-forming fluids is a prerequisite in deciphering the genesis of mineral deposits (Cao et al. 2020; Qiu et al. 2021). The brookite and anatase in the fine-grained matrix of altered porphyritic monzogranite formed pseudomorphs after magmatic titanite and at contacts with monazite, magnetite, and quartz, indicating that the lower temperature argillic alteration associated with late-stage mineralization was in an H<sub>2</sub>O-rich environment with a relatively high  $f_{O_2}$  (Broska et al. 2007; Huang et al. 2019; Xiao et al. 2021). This easily overlooked observation suggests that TiO<sub>2</sub> polymorphs can be produced by varying degrees of hydrothermal fluids modification in a porphyry system (Plavsa et al. 2018). The texture and geochemistry of the type-II rutile indicate that the hydrothermal fluid during potassic alteration was more oxidized, preceding the main mineralization stage. The widespread occurrence of the type-III rutile intergrown with sulfides formed during the main mineralization stage shows that Ti can be highly mobile in hydrothermal fluids during porphyry alteration. Furthermore, the enrichment of W in the type-III rutile indicates that these elements are highly mobile in the hydrothermal fluids in the presence of halogen-rich (F, Cl) aqueous fluids associated with the mineralization at Yulong.

In summary, the mineralizing hydrothermal fluids in the Yulong deposit had a high  $f_{O_2}$  at a high temperature and were rich in SO<sub>2</sub> and F. This resulted in the breakdown of pre-existing Ti-rich minerals and mobilizing relatively insoluble HFSEs. These ore-forming fluids are crucial for the formation of hydrothermal rutile in porphyry deposits.

### IMPLICATIONS

The textures, assemblages, and compositions of hydrothermal rutile forming contemporaneously with ore mineralization can

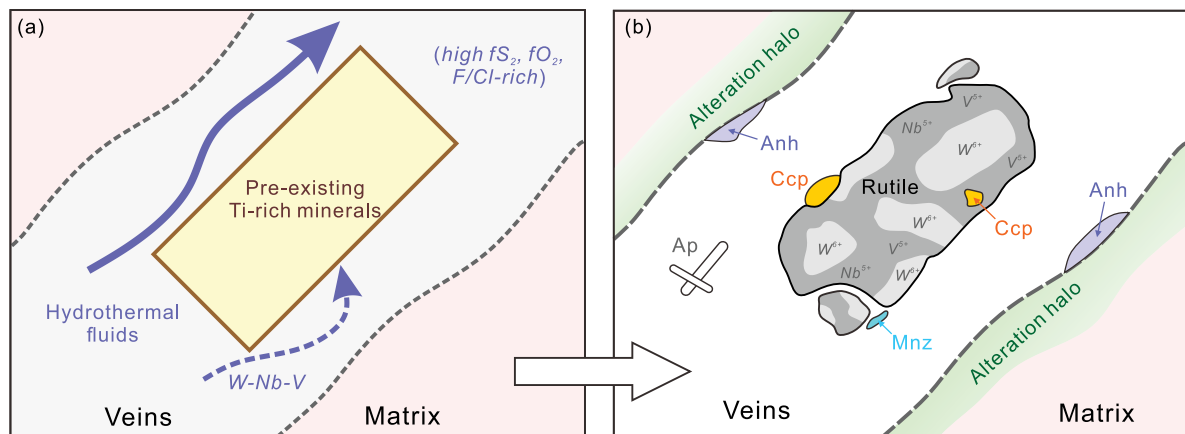


**FIGURE 12.** Model of rutile formation via replacement of pre-existing Ti-rich minerals. Flow of mineralizing fluids (arrows) can mobilize scarcely soluble elements, such as W, V, Nb. Abbreviations: Anh = anhydrite; Ap = apatite; Mnz = monazite. (Color online.)

provide clues and information regarding the genesis of hydrothermal processes during the growth of magmatic-hydrothermal deposits. The trace element composition of hydrothermal rutile can be used as a pathfinder for hydrothermal activity. The introduction of trace elements driven by hydrothermal alteration explains the variety of chemical compositions observed in natural hydrothermal rutile found in porphyry copper deposits. High-temperature ore-forming fluids with high oxygen fugacity and rich in  $\text{SO}_2$  and F can promote the introduction of relatively insoluble high field-strength elements and base metals (such as W) into the crystal structure of rutile. Consequently, the chemical or isotopic composition recorded in rutile provides comprehensive information allowing us to better understand the nature of hydrothermal fluids operating during the deposition of porphyry deposits. This in turn potentially allows us to define vectors toward the location of porphyry deposits. Geochemistry of hydrothermal rutile can be expected to provide additional insights into hydrothermal fluid compositions responsible for different mineralization styles. In addition, it has been identified that anatase and brookite (rather than rutile) replaced titanite during low-temperature argillic alteration. Thus, detailed and correct identification of  $\text{TiO}_2$  polymorphs may help better understand hydrothermal processes, particularly using rutile geochemistry as a vector toward mineralization.

#### ACKNOWLEDGMENTS

We thank Diana Zivak, University of Adelaide, Australia, and the anonymous journal reviewers for their critical reviews and constructive comments. We are also grateful to Associate Editor Paul Tomascak for their valuable help in handling this paper. We are grateful to Shentai Liu, the Engineer of Tibet Yulong Copper Co. Ltd., for his assistance during the field investigation.

#### FUNDING

This work was supported by the National Key Research and Development Project of China (Number 2020YFA0714802), the National Natural Science Foundation of China (Numbers 41872080), and the Most Special Fund from the State Key Laboratory of Geological Processes and Mineral Resources in China University of Geosciences (Beijing) of China (Number MSFGPMR201804).

#### REFERENCES CITED

- Adlaka, E.E., Hattori, K., Kerr, M.J., and Boucher, B.M. (2020) The origin of Ti-oxide minerals below and within the eastern Athabasca Basin, Canada. *American Mineralogist*, 105, 1875–1888, <https://doi.org/10.2138/am-2020-7235>.
- Angari, A., Reddy, S.M., Plavsa, D., Fougereuse, D., Clark, C., Roberts, M., and Johnson, T.E. (2019) Antimony in rutile as a pathfinder for orogenic gold deposits. *Ore Geology Reviews*, 106, 1–11, <https://doi.org/10.1016/j.oregeorev.2019.01.018>.
- Angari, A., Plavsa, D., Reddy, S.M., Olierook, H., and Kylander-Clark, A. (2020) Compositional modification and trace element decoupling in rutile: Insight from the Capricorn Orogen, western Australia. *Precambrian Research*, 345, 105772, <https://doi.org/10.1016/j.precamres.2020.105772>.
- Baur, W.H. (2007) The rutile type and its derivatives. *Crystallography Reviews*, 13, 65–113, <https://doi.org/10.1080/08893110701433435>.
- Borges, P.D., Scolfaro, L., and Assali, L.V.C. (2015) Complex centers of hydrogen in tin dioxide. *Theoretical Chemistry Accounts*, 134, 131, <https://doi.org/10.1007/s00214-015-1735-2>.
- Bromley, G.D., Hilaiert, N., and McCammon, C. (2004) Solubility of hydrogen and ferric iron in rutile and  $\text{TiO}_2$  (II): Implications for phase assemblages during ultra-high pressure metamorphism and for the stability of silica polymorphs in the lower mantle. *Geophysical Research Letters*, 31, L04610, <https://doi.org/10.1029/2004GL019430>.
- Broska, I., Harlov, D., Tropper, P., and Siman, P. (2007) Formation of magmatic titanite and titanite-ilmenite phase relations during granite alteration in the Tribeč Mountains, Western Carpathians, Slovakia. *Lithos*, 95, 58–71, <https://doi.org/10.1016/j.lithos.2006.07.012>.
- Cabral, A.R., Rios, F.J., de Oliveira, L.A.R., de Abreu, F.R., Lehmann, B., Zack, T., and Lauek, F. (2015) Fluid-inclusion microthermometry and the Zr-in-rutile thermometer for hydrothermal rutile. *International Journal of Earth Sciences*, 104, 513–519, <https://doi.org/10.1007/s00531-014-1120-8>.
- Cao, M.J., Hollings, P., Evans, N.J., Cooke, D.R., McInnes, B.I.A., Zhao, K.D., Qin, K.Z., Li, D.F., and Sweet, G. (2020) In situ elemental and Sr isotopic characteristics of magmatic to hydrothermal minerals from the Black Mountain porphyry deposit, Baguio district, Philippines. *Economic Geology and the Bulletin of the Society of Economic Geologists*, 115, 927–944, <https://doi.org/10.5382/econgeo.4701>.
- Carruzzo, S., Clarke, D.B., Pelrine, K.M., and MacDonald, M.A. (2006) Texture, composition, and origin of rutile in the South Mountain Batholith, Nova Scotia. *Canadian Mineralogist*, 44, 715–729, <https://doi.org/10.2113/gscanmin.44.3.715>.
- Chang, J., Li, J.W., Selby, D., Liu, J.C., and Deng, X.D. (2017) Geological and chronological constraints on the long-lived eocene Yulong porphyry Cu-Mo Deposit, Eastern Tibet: Implications for the lifespan of giant porphyry Cu deposits. *Economic Geology*, 112, 1719–1746, <https://doi.org/10.5382/econgeo.2017.4527>.
- Chang, J., Li, J.W., and Audétat, A. (2018) Formation and evolution of multistage magmatic-hydrothermal fluids at the Yulong porphyry Cu-Mo deposit, eastern Tibet: Insights from LA-ICP-MS analysis of fluid inclusions. *Geochimica et Cosmochimica Acta*, 232, 181–205, <https://doi.org/10.1016/j.gca.2018.04.009>.
- Chen, Q., Wang C.M., Bagas, L., Zhang, Z.C., and Du, B. (2021) Time scales of multistage magma-related hydrothermal fluids at the giant Yulong porphyry Cu-Mo deposit in eastern Tibet: Insights from titanium diffusion in quartz. *Ore Geology Reviews*, 139(A), 104459, <https://doi.org/10.1016/j.oregeorev.2021.104459>.
- Cherniak, D.J. (2000) Pb diffusion in rutile. *Contributions to Mineralogy and Petrology*, 139, 198–207, <https://doi.org/10.1007/PL00007671>.
- Chevychev, V.Y., Zaraisky, G.P., Borisovskii, S.E., and Borkov, D.A. (2005) Effect of melt composition and temperature on the partitioning of Ta, Nb, Mn, and F between granitic (alkaline) melt and fluorine-bearing aqueous fluid: Fractionation of Ta and Nb and conditions of ore formation in rare-metal granites. *Petrology*, 13, 305–321.
- Chiaradia, M., Schaltegger, U., and Spikings, R. (2014) Time scales of mineral systems—advances in understanding over the past decade. *Society of Economic Geologists, Special Publication* 18, 37–58.
- Clark, J.R. and Williams-Jones, A.E. (2004) Rutile as a potential indicator mineral for metamorphosed metallic ore deposits. *Rapport Final de DIVEX, Sous-projet SC2: Montreal*, p. 17.
- Czarnanske, G.K., Force, E.R., and Moore, W.J. (1981) Some geologic and potential resource aspects of rutile in porphyry copper deposits. *Economic Geology and the Bulletin of the Society of Economic Geologists*, 76, 2240–2246, <https://doi.org/10.2113/gsecongeo.76.8.2240>.
- Deng, J., Wang, C.M., Bagas, L., Selvaraja, V., Jeon, H., Wu, B., and Yang, L.F. (2017) Insights into ore genesis of the Jinding Zn-Pb deposit, Yunnan Province, China: Evidence from Zn and in situ S isotopes. *Ore Geology Reviews*, 90, 943–957, <https://doi.org/10.1016/j.oregeorev.2016.10.036>.
- Deng, J., Wang, C.M., Zi, J.W., Xia, R., and Li, Q. (2018) Constraining subduction-collision processes of the Pale-Tethys along The Changning-Menglian Suture: New zircon U-Pb ages and Sr-Nd-Pb-Hf-O isotopes of the Lincang Batholith. *Gondwana Research*, 62, 75–92, <https://doi.org/10.1016/j.gr.2017.10.008>.
- Ewing, T.A., Hermann, J., and Rubatto, D. (2013) The robustness of the Zr-in-rutile and Ti-in-zircon thermometers during high-temperature metamorphism (Ivrea-Verbano Zone, northern Italy). *Contributions to Mineralogy and Petrology*, 165, 757–779, <https://doi.org/10.1007/s00410-012-0834-5>.
- Feng, H.X., Shen, P., Zhu, R.X., Ma, G., Li, J.P., and Li, J. (2020) SIMS U-Pb dating of vein-hosted hydrothermal rutile and carbon isotope of fluids in the Wulong lode gold deposit, NE China: Linking gold mineralization with orogenic destruction. *Ore Geology Reviews*, 127, 103838, <https://doi.org/10.1016/j.oregeorev.2020.103838>.
- Gao, X.Y., Zheng, Y.F., Xia, X.P., and Chen, Y.X. (2014) U-Pb ages and trace elements of metamorphic rutile from ultrahigh-pressure quartzite in the Sulu orogeny. *Geochimica et Cosmochimica Acta*, 143, 87–114, <https://doi.org/10.1016/j.gca.2014.04.032>.
- Hart, E., Storey, C., Harley, S.L., and Fowler, M. (2018) A window into the lower crust: Trace element systematics and the occurrence of inclusions/intergrowths in granulite-facies rutile. *Gondwana Research*, 59, 76–86, <https://doi.org/10.1016/j.gr.2018.02.021>.
- Hou, Z.Q., Ma, H.W., Khin, Z., Zhang, Y.Q., Wang, M.J., Wang, Z., Pan, G.T., and Tang, R.L. (2003) The Himalayan Yulong porphyry copper belt: Product of large-scale strike-slip faulting in eastern Tibet. *Economic Geology and the Bulletin of the Society of Economic Geologists*, 98, 125–145.
- Hou, Z.Q., Zeng, P.S., Gao, Y.F., Du, A.D., and Fu, D.M. (2006) Himalayan Cu-Mo-Au mineralization in the eastern Indo-Asian collision zone: Constraints from Re-Os dating of molybdenite. *Mineralium Deposita*, 41, 33–45, <https://doi.org/10.1007/s00126-005-0038-2>.
- Hou, Z.Q., Yang, Z.M., Lu, Y.J., Kemp, A., Zheng, Y.C., Li, Q.Y., Tang, J.X., Yang, Z.S., and Duan, L.F. (2015) A genetic linkage between subduction- and collision-related porphyry Cu deposits in continental collision zones. *Geology*, 43, 247–250, <https://doi.org/10.1130/G36362.1>.
- Huang, M.L., Bi, X.W., Richards, J.P., Hu, R.Z., Xu, L.L., Gao, J.F., Zhu, J.J., and Zhang, X.C. (2019) High water contents of magmas and extensive fluid exsolution during the formation of the Yulong porphyry Cu-Mo deposit, eastern

- Tibet. *Journal of Asian Earth Sciences*, 176, 168–183, <https://doi.org/10.1016/j.jseas.2019.02.008>.
- Klein, C. and Dutrow, B. (2007) *Manual of Mineral Science*, 23rd ed., 716 p. Wiley.
- Li, J.X., Qin, K.Z., Li, G.M., Cao, M.J., Xiao, B., Chen, L., Zhao, J.X., Evans, N.J., and McInnes, B.I.A. (2012) Petrogenesis and thermal history of the Yulong porphyry copper deposit, Eastern Tibet: Insights from U-Pb and U-Th/He dating, and zircon Hf isotope and trace element analysis. *Mineralogy and Petrology*, 105, 201–221, <https://doi.org/10.1007/s00710-012-0211-0>.
- Liang, H.Y., Campbell, I.H., Allen, C., Sun, W.D., Liu, C.Q., Yu, H.X., Xie, Y.W., and Zhang, Y.Q. (2006) Zircon  $Ce^{4+}/Ce^{3+}$  ratios and ages for Yulong ore-bearing porphyries in eastern Tibet. *Mineralium Deposita*, 41, 152–159, <https://doi.org/10.1007/s00126-005-0047-1>.
- Losos, Z. and Beran, A. (2004) OH defects in cassiterite. *Mineralogy and Petrology*, 81, 219–234, <https://doi.org/10.1007/s00710-004-0040-x>.
- Lu, Y.J., Loucks, R.B., Fiorentini, M.L., Yang, Z.M., and Hou, Z.Q. (2015) Fluid flux melting generated post-collisional high-Sr/Y copper ore-forming water-rich magmas in Tibet. *Geology*, 43, 583–586, <https://doi.org/10.1130/G36734.1>.
- Ludwig, K.R. (2008) *A User's Manual for Isoplot 3.6: A Geochronological Toolkit for Microsoft Excel*. Berkeley Geochronological Center.
- Luvizotto, G.L. and Zack, T. (2009) Nb and Zr behavior in rutile during high-grade metamorphism and retrogression: An example from the Ivrea-Verbano Zone. *Chemical Geology*, 261, 303–317, <https://doi.org/10.1016/j.chemgeo.2008.07.023>.
- Majzlan, J., Bolanz, R., Göttlicher, J., Mikus, T., Milovská, S., Caplovicová, M., Števkó, M., Rössler, C., and Matthes, C. (2021) Incorporation mechanism of tungsten in W-Fe-Cr-V-bearing rutile. *American Mineralogist*, 106, 609–619, <https://doi.org/10.2138/am-2021-7653>.
- Maldener, J., Rauch, F., Gavranic, M., and Beran, A. (2001) OH absorption coefficients of rutile and cassiterite deduced from nuclear reaction analysis and FTIR spectroscopy. *Mineralogy and Petrology*, 71, 21–29, <https://doi.org/10.1007/s007100170043>.
- Meinhold, G. (2010) Rutile and its applications in earth sciences. *Earth-Science Reviews*, 102, 1–28, <https://doi.org/10.1016/j.earscirev.2010.06.001>.
- Mercer, C.N. and Reed, M.H. (2013) Porphyry Cu-Mo stockwork formation by dynamic, transient hydrothermal pulses: Mineralogical insights from the deposit at Butte, Montana. *Economic Geology and the Bulletin of the Society of Economic Geologists*, 108, 1347–1377, <https://doi.org/10.2113/econgeo.108.6.1347>.
- Meyer, M., John, T., Brandt, S., and Klemd, R. (2011) Trace element composition of rutile and the application of Zr-in-rutile thermometry to UHT metamorphism (Europa complex, NW Namibia). *Lithos*, 126, 388–401, <https://doi.org/10.1016/j.lithos.2011.07.013>.
- Moore, J., Beinlich, A., Porter, J.K., Talavera, C., Berndt, J., Piazzolo, S., Austrheim, H., and Putnis, A. (2020) Microstructurally controlled trace element (Zr, U-Pb) concentrations in metamorphic rutile: An example from the amphibolites of the Bergen Arcs. *Journal of Metamorphic Geology*, 38, 103–127, <https://doi.org/10.1111/jmg.12514>.
- Murad, E., Cashion, J.D., Noble, C.J., and Pilbrow, J.R. (1995) The chemical state of Fe in rutile from an albite in Norway. *Mineralogical Magazine*, 59, 557–560, <https://doi.org/10.1180/minmag.1995.059.396.17>.
- Okay, N., Zack, T., Okay, A.I., and Barth, M. (2011) Sinistral transport along the Trans-European Suture Zone: Detrital zircon-rutile geochronology and sandstone petrography from the Carboniferous flysch of the Pontides. *Geological Magazine*, 148, 380–403, <https://doi.org/10.1017/S0016756810000804>.
- Paton, C., Hellstrom, J., Paul, B., Woodhead, J., and Hergt, J. (2011) Iolite: Free-ware for the visualization and processing of mass spectrometric data. *Journal of Analytical Atomic Spectrometry*, 26, 2508–2518, <https://doi.org/10.1039/c1ja10172b>.
- Pe-Piper, G., Nagle, J., Piper, D., and McFarlane, C. (2019) Geochronology and trace element mobility in rutile from a Carboniferous syenite pegmatite and the role of halogens. *American Mineralogist*, 104, 501–513, <https://doi.org/10.2138/am-2019-6668>.
- Pereira, I., Storey, C., Darling, J., Lana, C., and Alkmim, A.R. (2019) Two billion years of evolution enclosed in hydrothermal rutile: Recycling of the São Francisco Craton Crust and constraints on gold remobilisation processes. *Gondwana Research*, 68, 69–92, <https://doi.org/10.1016/j.gr.2018.11.008>.
- Plavsa, D., Reddy, S.M., Agangi, A., Clark, C., Kylander-Clark, A., and Tiddy, C.J. (2018) Microstructural, trace element and geochronological characterization of TiO<sub>2</sub> polymorphs and implications for mineral exploration. *Chemical Geology*, 476, 130–149, <https://doi.org/10.1016/j.chemgeo.2017.11.011>.
- Qiu, K.F., Yu, H.C., Hetherington, C., Huang, Y.Q., Yang, T., and Deng, J. (2021) Tourmaline composition and boron isotope signature as a tracer of magmatic-hydrothermal processes. *American Mineralogist*, 106, 1033–1044, <https://doi.org/10.2138/am-2021-7495>.
- Rabbia, O. and Hernández, L.B. (2012) Mineral chemistry and potential applications of natural-multi-doped hydrothermal rutile from porphyry copper deposits. In I.M. Low, Ed., *Rutile: Properties, Synthesis and Application*, p. 209–228. Nova Science Publishers.
- Rabbia, O.M., Hernández, L.B., French, D.H., King, R.W., and Ayers, J.C. (2009) The El Teniente porphyry Cu-Mo deposit from a hydrothermal rutile perspective. *Mineralium Deposita*, 44, 849–866, <https://doi.org/10.1007/s00126-009-0252-4>.
- Rapp, J.F., Klemme, S., Butler, I.B., and Harley, S.L. (2010) Extremely high solubility of rutile in chloride and fluoride-bearing metamorphic fluids: An experimental investigation. *Geology*, 38, 323–326, <https://doi.org/10.1130/G30753.1>.
- Reznitsky, L.Z., Sklyarov, E.V., Suvorova, L.F., Barash, I.G., and Karmanov, N.S. (2017) V-Cr-Nb-W-bearing rutile in metamorphic rocks of the Slyudyanka complex, southern Baikal region. *Geology of Ore Deposits*, 59, 707–719, <https://doi.org/10.1134/S1075701517080086>.
- Rösel, D., Zack, T., and Moller, A. (2019) Interpretation and significance of combined trace element and U-Pb isotopic data of detrital rutile: A case study from late Ordovician sedimentary rocks of Saxo-Thuringia, Germany. *International Journal of Earth Sciences*, 108, 1–25, <https://doi.org/10.1007/s00531-018-1643-5>.
- Santos, M.M., Lana, C., Scholz, R., Buick, I.S., Kamo, S.L., Corfú, F., and Queiroga, G. (2020) LA-ICP-MS U-Pb dating of rutiles associated with hydrothermal mineralization along the southern Araçuaí Belt, SE Brazil. *Journal of Asian Earth Sciences*, 99, 1–15.
- Schirra, M. and Laurent, O. (2021) Petrochronology of hydrothermal rutile in mineralized porphyry Cu systems. *Chemical Geology*, 581, 120407, <https://doi.org/10.1016/j.chemgeo.2021.120407>.
- Scott, K.M. (2005) Rutile geochemistry as a guide to porphyry Cu-Au mineralization, North Parkes, New South Wales, Australia. *Geochemistry Exploration Environment Analysis*, 5, 247–253, <https://doi.org/10.1144/1467-7873/03-055>.
- Scott, K.M., Radford, N.W., Hough, R.M., and Reddy, S.M. (2011) Rutile compositions in the Kalgoorlie Goldfields and their implications for exploration. *Australian Journal of Earth Sciences*, 58, 803–812, <https://doi.org/10.1080/08120099.2011.600334>.
- Şengün, F. and Zack, T. (2016) Trace element composition of rutile and Zr-in-rutile thermometry in meta-ophiolitic rocks from the Kazağ Massif, NW Turkey. *Mineralogy and Petrology*, 110, 547–560, <https://doi.org/10.1007/s00710-016-0433-7>.
- Şengün, F., Zack, T., and Dunkl, I. (2020) Provenance of detrital rutiles from the Jurassic sandstones in the Central Sakarya Zone, NW Turkey: U-Pb ages and trace element geochemistry. *Chemie der Erde*, 80, 125667, <https://doi.org/10.1016/j.chemer.2020.125667>.
- Shannon, R.D. (1976) Revised effective ionic radii and systematic studies of interatomic distances in halides and chalcogenides. *Acta Crystallographica*, 32, 751–767, <https://doi.org/10.1107/S0567739476001551>.
- Smith, S.J., Stevens, R., Liu, S.F., Li, G.S., Navrotsky, A., Boerio-Goates, J., and Woodfield, B.F. (2009) Heat capacities and thermodynamic functions of TiO<sub>2</sub> anatase and rutile: Analysis of phase stability. *American Mineralogist*, 94, 236–243, <https://doi.org/10.2138/am.2009.3050>.
- Sun, M.Y., Monecke, T., Reynolds, T.J., and Yang, Z.M. (2021) Understanding the evolution of magmatic-hydrothermal systems based on microtextural relationships, fluid inclusion petrography, and quartz solubility constraints: Insights into the formation of the Yulong Cu-Mo porphyry deposit, eastern Tibetan Plateau, China. *Mineralium Deposita*, 56, 823–842, <https://doi.org/10.1007/s00126-020-01003-6>.
- Tang, R.L. and Luo, H.S. (1995) *The geology of Yulong porphyry copper (molybdenum) ore belt, Xizang (Tibet)*, 320 p. Geological Publishing House.
- Tomkins, H.S., Powell, R., and Ellis, D.J. (2007) The pressure dependence of the zirconium-in-rutile thermometer. *Journal of Metamorphic Geology*, 25, 703–713, <https://doi.org/10.1111/j.1525-1314.2007.00724.x>.
- Triebold, S., Luvizotto, G.L., Tolosana-Delgado, R., Zack, T., and von Eynatten, H. (2011) Discrimination of TiO<sub>2</sub> polymorphs in sedimentary and metamorphic rocks. *Contributions to Mineralogy and Petrology*, 161, 581–596, <https://doi.org/10.1007/s00410-010-0551-x>.
- Ver Hoeve, T.J., Scoates, J.S., Wall, C.J., Weis, D., and Amini, M. (2018) A temperature composition framework for crystallization of fractionated interstitial melt in the Bushveld complex from trace element characteristics of zircon and rutile. *Journal of Petrology*, 59, 1383–1416, <https://doi.org/10.1093/petrology/egy066>.
- Wang, C.H., Tang, J.X., Chen, J.P., Hao, J.H., Gao, Y.M., Liu, Y.W., Fan, T., Zhang, Q.Z., Ying, L.J., and Chen, Z.J. (2009) Chronological research of Yulong copper-molybdenum porphyry deposit. *Acta Geologica Sinica*, 83, 1445–1455. (In Chinese with English abstract)
- Wang, C.M., Deng, J., Carranza, E.J.M., and Santosh, M. (2014) Tin metallogenesis associated with granitoids in the southwestern Sanjiang Tethyan Domain: Nature, deposit types, and tectonic setting. *Gondwana Research*, 26, 576–593, <https://doi.org/10.1016/j.gr.2013.05.005>.
- Wang, C.M., Bagas, L., Lu, Y.J., Santosh, M., Du, B., and McCuaig, T.C. (2016) Terrane boundary and spatio-temporal distribution of ore deposits in the Sanjiang Tethyan Orogen: Insights from zircon Hf-isotopic mapping. *Earth-Science Reviews*, 156, 39–65, <https://doi.org/10.1016/j.earscirev.2016.02.008>.
- Wang, C.M., Bagas, L., Chen, J.Y., Yang, L.F., Zhang, D., Du, B., and Shi, K.X. (2018a) The genesis of the Liancheng Cu-Mo deposit in the Lanping Basin of SW China: Constraints from geology, fluid inclusions, and Cu-S-H-O isotopes. *Ore Geology Reviews*, 92, 113–128, <https://doi.org/10.1016/j.oregeorev.2017.11.012>.
- Wang, R., Weinberg, R.F., Collins, W.J., Richards, J.P., and Zhu, D.C. (2018b)

- Origin of post-collisional magmas and formation of porphyry Cu deposits in southern Tibet. *Earth-Science Reviews*, 181, 122–143, <https://doi.org/10.1016/j.earscirev.2018.02.019>.
- Wang, C.M., Rao, S.C., Shi, K.X., Bagas, L., Chen, Q., Zhu, J.X., Duan, H.Y., and Liu, L.J. (2021) Rutile in amphibolite facies metamorphic rocks: A rare example from the East Qinling Orogen, China. *Applied Sciences (Basel, Switzerland)*, 11, 8756, <https://doi.org/10.3390/app11188756>.
- Williams, I.S. (1998) U-Th-Pb geochronology by ion microprobe. In M.A. McKibben, W.C. Shanks, and W.I. Ridley, Eds., *Applications of microanalytical techniques to understanding mineralizing processes*. *Reviews in Economic Geology*, 7, 35, <https://doi.org/10.5382/Rev.07.01>.
- Win, M.M., Enami, M., Kato, T., and Thu, Y.K. (2017) A mechanism for Nb incorporation in rutile and application of Zr-in-rutile thermometry: A case study from granulite facies paragneisses of the Mogok metamorphic belt, Myanmar. *Mineralogical Magazine*, 81, 1503–1521, <https://doi.org/10.1180/minmag.2017.081.014>.
- Xiao, X., Zhou, T.F., White, N.C., Zhang, L.J., Fan, Y., and Chen, X.F. (2021) Multiple generations of titanites and their geochemical characteristics record the magmatic-hydrothermal processes and timing of the Dongguashan porphyry-skarn Cu-Au system, Tongling district, Eastern China. *Mineralium Deposita*, 56, 363–380, <https://doi.org/10.1007/s00126-020-00962-0>.
- Yang, Z.M. and Cooke, D.R. (2019) Porphyry copper deposits in China. In Z.S. Chang and R.J. Goldfarb, Eds., *Mineral Deposits of China*, p. 133–187. Society of Economic Geologists, Special Publication. Society of Economic Geologists.
- Yang, Z.M., Hou, Z.Q., Xu, J.F., Bian, X.F., Wang, G.R., Yang, Z.S., Tian, S.H., Liu, Y.C., and Wang, Z.L. (2014) Geology and origin of the post-collisional Narigongma porphyry Cu-Mo deposit, southern Qinghai, Tibet. *Gondwana Research*, 26, 536–556, <https://doi.org/10.1016/j.gr.2013.07.012>.
- Zack, T. and Kooijman, E. (2017) Petrology and geochronology of rutile. *Reviews in Mineralogy and Geochemistry*, 83, 443–467, <https://doi.org/10.2138/rmg.2017.83.14>.
- Zack, T., Kronz, A., Foley, S.F., and Rivers, T. (2002) Trace element abundances in rutiles from eclogites and associated garnet mica schists. *Chemical Geology*, 184, 97–122, [https://doi.org/10.1016/S0009-2541\(01\)00357-6](https://doi.org/10.1016/S0009-2541(01)00357-6).
- Zack, T., Moraes, R., and Kronz, A. (2004) Temperature dependence of Zr in rutile: Empirical calibration of a rutile thermometer. *Contributions to Mineralogy and Petrology*, 148, 471–488, <https://doi.org/10.1007/s00410-004-0617-8>.
- Zhang, L., Wu, J.L., Tu, J.R., Wu, D., Li, N., Xia, X.P., and Ren, Z.Y. (2020) RMJG Rutile: A new natural reference material for microbeam U-Pb dating and Hf isotopic analysis. *Geostandards and Geoanalytical Research*, 44, 133–145, <https://doi.org/10.1111/ggr.12304>.

MANUSCRIPT RECEIVED JANUARY 16, 2022

MANUSCRIPT ACCEPTED JULY 9, 2022

ACCEPTED MANUSCRIPT ONLINE JULY 22, 2022

MANUSCRIPT HANDLED BY PAUL TOMASCAK

### Endnote:

<sup>1</sup>Deposit item AM-23-68453, Online Materials. Deposit items are free to all readers and found on the MSA website, via the specific issue's Table of Contents (go to [http://www.minsocam.org/MSA/AmMin/TOC/2023/Jun2023\\_data/Jun2023\\_data.html](http://www.minsocam.org/MSA/AmMin/TOC/2023/Jun2023_data/Jun2023_data.html)).